MIT Libraries | DSpace@MIT

MIT Open Access Articles

The Observed State of the Energy Budget in the Early Twenty-First Century

The MIT Faculty has made this article openly available. ***Please share*** how this access benefits you. Your story matters.

Citation: L'Ecuyer, Tristan S., H. K. Beaudoing, M. Rodell, W. Olson, B. Lin, S. Kato, C. A. Clayson, et al. "The Observed State of the Energy Budget in the Early Twenty-First Century." J. Climate 28, no. 21 (November 2015): 8319–8346. © 2015 American Meteorological Society

As Published: http://dx.doi.org/10.1175/JCLI-D-14-00556.1

Publisher: American Meteorological Society

Persistent URL: http://hdl.handle.net/1721.1/108507

Version: Final published version: final published article, as it appeared in a journal, conference proceedings, or other formally published context

Terms of Use: Article is made available in accordance with the publisher's policy and may be subject to US copyright law. Please refer to the publisher's site for terms of use.

Massachusetts Institute of Technology

The Observed State of the Energy Budget in the Early Twenty-First Century

TRISTAN S. L'ECUYER,[a] H. K. BEAUDOING,[b,c] M. RODELL,[b] W. OLSON,[d] B. LIN,[e] S. KATO,[e] C. A. CLAYSON,[f]
E. WOOD,[g] J. SHEFFIELD,[g] R. ADLER,[c] G. HUFFMAN,[b] M. BOSILOVICH,[b] G. GU,[b] F. ROBERTSON,[h]
P. R. HOUSER,[i] D. CHAMBERS,[j] J. S. FAMIGLIETTI,[k] E. FETZER,[k] W. T. LIU,[k] X. GAO,[l]
C. A. SCHLOSSER,[l] E. CLARK,[m] D. P. LETTENMAIER,[m] AND K. HILBURN[n]

[a] *University of Wisconsin–Madison, Madison, Wisconsin*
[b] *NASA Goddard Space Flight Center, Greenbelt, Maryland*
[c] *Earth System Science Interdisciplinary Center, University of Maryland, College Park, College Park, Maryland*
[d] *Joint Center for Earth Systems Technology/University of Maryland, Baltimore County, Baltimore, Maryland*
[e] *NASA Langley Research Center, Norfolk, Virginia*
[f] *Woods Hole Oceanographic Institution, Woods Hole, Massachusetts*
[g] *Princeton University, Princeton, New Jersey*
[h] *NASA Marshall Space Flight Center, Huntsville, Alabama*
[i] *George Mason University, Fairfax, Virginia*
[j] *University of South Florida, St. Petersburg, Florida*
[k] *NASA Jet Propulsion Laboratory, Pasadena, California*
[l] *Massachusetts Institute of Technology, Cambridge, Massachusetts*
[m] *University of Washington, Seattle, Washington*
[n] *Remote Sensing Systems, Santa Rosa, California*

(Manuscript received 23 July 2014, in final form 17 June 2015)

ABSTRACT

New objectively balanced observation-based reconstructions of global and continental energy budgets and their seasonal variability are presented that span the golden decade of Earth-observing satellites at the start of the twenty-first century. In the absence of balance constraints, various combinations of modern flux datasets reveal that current estimates of net radiation into Earth's surface exceed corresponding turbulent heat fluxes by 13–24 W m^{-2}. The largest imbalances occur over oceanic regions where the component algorithms operate independent of closure constraints. Recent uncertainty assessments suggest that these imbalances fall within anticipated error bounds for each dataset, but the systematic nature of required adjustments across different regions confirm the existence of biases in the component fluxes. To reintroduce energy and water cycle closure information lost in the development of independent flux datasets, a variational method is introduced that explicitly accounts for the relative accuracies in all component fluxes. Applying the technique to a 10-yr record of satellite observations yields new energy budget estimates that simultaneously satisfy all energy and water cycle balance constraints. Globally, 180 W m^{-2} of atmospheric longwave cooling is balanced by 74 W m^{-2} of shortwave absorption and 106 W m^{-2} of latent and sensible heat release. At the surface, 106 W m^{-2} of downwelling radiation is balanced by turbulent heat transfer to within a residual heat flux into the oceans of 0.45 W m^{-2}, consistent with recent observations of changes in ocean heat content. Annual mean energy budgets and their seasonal cycles for each of seven continents and nine ocean basins are also presented.

1. Introduction

Spatial and temporal variations in the flows of energy between the surface, the atmosphere, and space play a central role in establishing the large-scale atmosphere and ocean circulation patterns that ultimately drive both weather and climate (e.g., Hartmann et al. 1984; Lau and Peng 1987; Slingo and Slingo 1988, 1991; Lee et al. 2001; Schumacher et al. 2004). The sensitivity of the climate system to external forcings is therefore governed by the energy imbalances they induce and the partitioning of these imbalances between the atmosphere, ocean, and cryosphere (Trenberth 2009; Trenberth et al. 2014). As a result, several recently documented biases in climate

---

Denotes Open Access content.

Corresponding author address: Tristan L'Ecuyer, University of Wisconsin–Madison, 1225 W. Dayton St., Madison, WI 53574.
E-mail: tristan@aos.wisc.edu

DOI: 10.1175/JCLI-D-14-00556.1

© 2015 American Meteorological Society

models, such as insufficient low cloud cover in subtropical subsidence regions (Kay et al. 2012), warm sea surface temperature (SST) biases in the southeast Pacific (Yu and Mechoso 1999; Dai et al. 2003), the presence of a ubiquitous tropical rainband south of the equator (Li et al. 2004; Masunaga and L'Ecuyer 2010), premature onset of deep convection (particularly over land) (Davis et al. 2003; Dai and Trenberth 2004; Grabowski et al. 2006), and underestimates of the Walker circulation response to El Niño (L'Ecuyer and Stephens 2007; Su and Jiang 2013), are likely connected to errors in the representation of energy flows in these models. The need to resolve these biases to improve future climate predictions motivates the development of accurate observationally based benchmarks of energy flows to evaluate and refine model physics (Bony et al. 2006).

Characterizing energy exchanges between the surface, the atmosphere, and space from observations has been the subject of vigorous research for more than a century (Abbot and Fowle 1908; Dines 1917). It was not until the late twentieth century, however, that satellite observations revolutionized our understanding of Earth's radiative balance by providing a unique global perspective on the spatial distribution of incoming and outgoing radiation at the top of the atmosphere (TOA). Early satellite studies demonstrated that Earth was darker and warmer than previously believed and that there was a stronger gradient of absorbed solar energy between the tropics and the midlatitudes (Vonder Haar and Suomi 1969; Vonder Haar et al. 1972). Following these initial discoveries, satellite observations with improved calibration and increased spatial and temporal resolution have played a central role in refining reconstructions of Earth's energy balance (e.g., Budyko 1974; Liou 1980; Peixoto and Oort 1992; Hartmann 1994; Rossow et al. 1995; Kiehl and Trenberth 1997; Zhang et al. 2004; and references therein).

The last decade can be considered a golden era in satellite Earth observation, especially for observations of direct relevance to Earth's energy budget. Clouds and the Earth's Radiant Energy System (CERES) instruments aboard the Tropical Rainfall Measuring Mission (TRMM), *Terra*, and *Aqua* satellites, for example, have provided improved observations of the exchange of longwave and shortwave radiation at the TOA (Wielicki et al. 1996; Loeb et al. 2001). When coupled with water vapor estimates from the Atmospheric Infrared Sounder (AIRS) and cloud and aerosol information from the Moderate Resolution Imaging Spectroradiometer (MODIS), *CloudSat*, and the *Cloud–Aerosol Lidar and Infrared Pathfinder Satellite Observations* (*CALIPSO*), these observations have also led to significant refinement to estimates of surface radiative fluxes (Stackhouse et al. 2001; L'Ecuyer et al. 2008; Kato et al. 2011). Likewise, the TRMM Microwave Imager (TMI) and precipitation radar (PR) as well as the Advanced Microwave Scanning Radiometer for Earth Observing System (EOS) (AMSR-E) aboard *Aqua* have provided new insights into the global distribution of latent heat release in precipitation and surface turbulent heat fluxes.

At the same time, a growing network of surface-based measurements has provided substantially better constraints on surface radiative and turbulent heat fluxes, such as the Baseline Surface Radiation Network (BSRN) (Ohmura et al. 1998) and FLUXNET (ORNL DAAC 2013). Likewise, recent advances in computing power have led to vast improvements in global atmospheric reanalyses through both increased resolution and the ability to assimilate extensive ground-based and satellite observations (Kalnay et al. 1996; Bosilovich et al. 2006; Onogi et al. 2007; Dee et al. 2011). Together, these advances have enabled new reconstructions of energy balance on global (Lin et al. 2008; Trenberth et al. 2009; Kato et al. 2011; Stephens et al. 2012b; Wild et al. 2013, 2015) and regional scales (Fasullo and Trenberth 2008a,b; Trenberth and Fasullo 2013b,c; Brown and Kummerow 2014) from various combinations of in situ observations, satellite datasets, and reanalyses.

Comparing the results of these complementary studies, however, reveals that imbalances exist in both the atmospheric and surface energy budgets when independent estimates of the component fluxes are combined because choices concerning the manner by which balance is achieved have resulted in substantial differences in downwelling longwave and shortwave radiation (DLR and DSR, respectively) and turbulent heat fluxes. Thus, while these reconstructions utilize high-quality inputs and make reasonable arguments for adjusting component fluxes based on either assessments against in situ datasets or satellite product intercomparisons, the lack of consensus among the resulting energy balance diagrams suggests there is room for improvement.

Since its inception, the mission of NASA's Energy and Water cycle Study (NEWS) has been to bring together complementary expertise and datasets from distinct missions to provide a comprehensive view of the water and energy cycle consequences of climate change (NSIT 2007). This study and its water cycle counterpart (Rodell et al. 2015) embrace the NEWS paradigm to develop new estimates of the current state of the water and energy cycles on global and continental scales using datasets from the recent golden age of satellite Earth observations. Drawing inspiration from the early efforts of Dines (1917), who combined the best estimates of several key radiative and nonradiative fluxes available at the time with carefully thought-out closure arguments to construct a comprehensive depiction of global energy balance, we introduce an objective approach for imposing closure constraints on disparate large-scale energy flux datasets derived from NASA's latest EOS satellites. Using well-documented variational methods (Rodgers 2000; Kalnay 2003), atmospheric and surface energy and water cycle closure equations are incorporated as soft constraints, yielding balanced energy budgets on continental scales with modest adjustments to each of the component fluxes based on rigorous estimates of their uncertainties. The approach has a number of advantages: 1) it provides a uniform framework for integrating satellite observations of energy and water fluxes from disparate sources; 2) it explicitly accounts for the relative uncertainties in all component fluxes; 3) it allows energy and water cycle balance constraints to be applied simultaneously, linked through latent heating; and 4) it provides quantitative metrics for evaluating how well balance could be achieved. The method does not, however, provide direct insights into specific sources of biases in any particular flux dataset. Furthermore, as with all methods for reconstructing energy budgets, the results are sensitive to the specific-input datasets, but care has been taken to use recent assessments of the uncertainties in the component fluxes from the literature to construct error bars that encompass the likely range of expected values.

The method is used to generate observation-based reconstructions of the energy budget both globally and on continental scales and document their seasonal cycles using several recently developed satellite datasets. These datasets are then used to assess the degree to which global and regional energy budgets balance on annual scales in section 3. An objective optimization approach is introduced in section 4 and used to generate closed global and regional energy budgets over the past decade that satisfy all relevant energy and water cycle constraints. Beyond accounting for the relative accuracy of each dataset, the approach simultaneously imposes energy and water cycle constraints on the system, providing a powerful tool for adding physical constraints that cannot be applied to individual datasets. It is argued that the resulting set of physically consistent energy budget and water cycle estimates [the latter reported in Rodell et al. (2015)] and associated error bars provide a measure of our ability to quantify the global energy and water cycles using modern satellite datasets.

2. Datasets

The goal of this study is to document observation-based reconstructions of energy budgets on time and space scales that begin to capture regional variability without exhibiting prohibitive sensitivity to measurement error. The analysis focuses on the decade from 2000 to 2009 to benefit from the availability of several new datasets developed during this golden age of Earth-observing satellites. A 10-yr period is adopted to smooth out interannual variations that may exert a strong influence over shorter time periods, with the caveat that it also ignores climate trends that may have occurred during this time. This time period corresponds to an apparent hiatus in global warming during which global temperatures remained relatively constant compared to trends in the previous two decades (Trenberth and Fasullo 2013a), but changes in other components of the climate system continued or accelerated. In particular, it has been documented that Greenland, Antarctica, and the glaciers along the Gulf of Alaska have been shedding mass at a total rate of 380 $\mathrm{km}^3\,\mathrm{yr}^{-1}$ (Luthcke et al. 2013). The impact of neglecting such trends on water and energy budgets is discussed below. Furthermore, owing to data availability at the time of analysis, some datasets span slightly different periods (e.g., 1998–2007), but an analysis of the magnitude of year-to-year variations in the component fluxes (not shown) reveals that the impact of these differences on the results is smaller than the uncertainties in each dataset.

For the reconstructions generated here to serve as a basis for future comparisons, the analysis is restricted to datasets for which justifiable error bars are available. Uncertainty estimates not only help establish the state of knowledge but they also supply critical input to the objective approach for introducing balance constraints introduced in section 4. However, assessing uncertainty poses a significant challenge for global satellite datasets because of the limited number of validation sites and the very different fields of view, sample volumes, and sensitivities of in situ instrumentation. The datasets listed in Table 1 were chosen because they span the period of interest and are sufficiently mature so that defensible uncertainty estimates have been published that account for both random and structural errors through comparisons against independent datasets, statistical validation against in situ observations, and rigorous sensitivity studies. Nevertheless, some decisions were made in compiling the final energy budgets presented here. When multiple estimates of a particular flux were available with no definitive method for determining relative accuracy, datasets were averaged to generate the final flux estimate. For other fluxes, a particular dataset was chosen based on its acceptance in the community as the observational standard. As this work was conducted under the auspices of NEWS, datasets provided by members of the NEWS team appear prominently in the analysis. NEWS datasets are widely available, have been the subject of comprehensive uncertainty assessment, undergo regular ongoing

TABLE 1. Data sources and associated documentation.

Parameter	Dataset	Relevant satellite inputs	References
Radiative fluxes	SRB	CERES, AVHRR	Gupta et al. (1999)
	ISCCP-FD	AVHRR	Zhang et al. (2004)
	2B-FLXHR-lidar	*CloudSat*, *CALIPSO*	Henderson et al. (2013)
	C3M	MODIS, AMSR-E, CERES, *CloudSat*, *CALIPSO*, MODIS	Kato et al. (2010); Kato et al. (2011)
Ocean turbulent heat fluxes	SeaFlux	SSM/I	Curry et al. (2004); Clayson et al. (2015, manuscript submitted to *Int. J. Climatol.*)
Land turbulent heat fluxes	Princeton ET	AIRS, CERES, MODIS, AVHRR	Vinukollu et al. (2011)
	MERRA	Numerous	Rienecker et al. (2011); Bosilovich et al. (2011)
	GLDAS	SSM/I, SSMIS, GOES-IR, TOVS, AIRS, TRMM, MODIS, AVHRR	Rodell et al. (2004b)
Atmospheric latent heating	GPCP v.2.2	SSM/I, SSMIS, GOES-IR, TOVS, AIRS	Adler et al. (2003); Huffman et al. (2009)

refinement, and facilitate consistency through common time and space grids. It is acknowledged that alternative datasets of similar quality exist, but at present it cannot be definitively demonstrated that these should be preferred over those chosen here. This does not mean that the chosen datasets have been anointed as the best nor should it be construed as a dismissal of others. To the contrary, considerable effort has been made to ensure that the associated error estimates accurately reflect the quality of the range of estimates that may be obtained from all viable alternatives. To these ends, the error estimates adopted below combine findings from several independent assessments that are largely decoupled from the specific data products used, instead representing the characteristics of each class of flux observations as a whole. Brief descriptions of each dataset used in this analysis are provided below, but the reader is directed to the cited literature for additional detail.

a. Radiative fluxes

The global average TOA solar insolation is taken to be 340.2 ± 0.1 $\mathrm{W\,m^{-2}}$ based on the recent total solar irradiance measurements from the Solar Radiation and Climate Experiment (SORCE) (Kopp and Lean 2011). Satellite measurements of other TOA and surface radiative fluxes derive from three NASA global radiation products: the CERES outgoing broadband flux product (Wielicki et al. 1996), the International Satellite Cloud Climatology Project Flux Data (ISCCP-FD) (Zhang et al. 2004), and the Global Energy and Water Cycle Experiment (GEWEX) Surface Radiation Budget (SRB) dataset (Gupta et al. 1999; Stackhouse et al. 2001). The ISCCP and SRB products calculate TOA and surface radiative fluxes based on satellite observations of the spatial distribution of clouds, aerosols, surface albedo, skin temperature, and emissivity constrained with atmospheric temperature and humidity profiles from the Television and Infrared Observation Satellite (TIROS) Operational Vertical Sounder (TOVS) and global atmospheric reanalyses, respectively. Each are compared against more direct measurements of broadband radiative fluxes at the TOA from CERES. A key property of these datasets is that the most relevant variables defining the propagation of radiation fluxes through the atmosphere, including cloud and aerosol optical properties, are obtained from multichannel narrowband satellite measurements. For the analyses that follow we adopt mean values of all TOA and surface radiative fluxes obtained by averaging ISCCP-FD and SRB datasets as the benchmark radiative fluxes. Note that the versions of these datasets used here employ a slightly larger value of the solar constant (342 $\mathrm{W\,m^{-2}}$) than the recent update provided by SORCE. This affects all shortwave fluxes, but the impacts are an order of magnitude smaller than the anticipated uncertainties in these fluxes.

Although they launched toward the end of the decade of interest for this study, the ability of *CloudSat* and *CALIPSO* to explicitly detect multilayered cloud systems and define cloud base height in most clouds (except those residing in the boundary layer) can be used to refine the error budgets of the ISCCP-FD and SRB datasets (Stephens et al. 2008; Winker et al. 2010; Rossow and Zhang 2010). The *CloudSat* 2B-FLXHR-lidar algorithm, for example, blends information from *CloudSat*, *CALIPSO*, MODIS, and AMSR-E to generate profiles of atmospheric radiative fluxes at high vertical and spatial resolutions (L'Ecuyer et al. 2008; Henderson et al. 2013). The algorithm supplements vertical distributions of cloud and precipitation water content and effective radii from *CloudSat*'s 94-GHz Cloud Profiling Radar (CPR) with characteristics of undetected thin cirrus and stratus clouds derived from *CALIPSO* and MODIS observations. Vertical profiles of aerosol type and optical depth are constrained using *CALIPSO* and surface albedo. Surface albedo and emissivity are assigned by coupling the International Geosphere–Biosphere Programme (IGBP) global land surface classification with estimates of snow and sea ice extent from the passive microwave-derived near-real-time equal-area scalable Earth grid (EASE-Grid) daily global ice concentration and snow extent (NISE) dataset (Nolin et al. 1998). These cloud, aerosol, and surface properties are combined with ancillary temperature and humidity profiles from the European Centre for Medium-Range Weather Forecasts (ECMWF) operational analyses and used to initialize a two-stream doubling-adding radiative transfer model to derive radiative flux profiles for each 1.4 km × 1.8 km *CloudSat* footprint at the 240-m vertical resolution of the CPR. Additional details concerning the approach and assessments of relevant uncertainties can be found in L'Ecuyer et al. (2008) and Henderson et al. (2013).

This study also makes use of the independent *CALIPSO*, *CloudSat*, CERES, and MODIS (CCCM) merged dataset data product that blends CERES and MODIS observations with cloud-top and -base height, liquid and ice water contents, extinction coefficients, and aerosol properties derived from merged *CloudSat*–*CALIPSO* observations. Cloud and aerosol properties are extracted from *CALIPSO* (Ed3 VFM, 5-km cloud profile, and 5-km aerosol layer) and *CloudSat* (Release 4 CLDCLASS and CWC-RO) products and averaged over the 20-km CERES footprint. The dataset itself, however, maintains the spatial resolution of original *CALIPSO* and *CloudSat* products. The process of merging *CALIPSO*- and *CloudSat*-derived cloud vertical profiles is explained in Kato et al. (2010), while the computation of irradiance profiles is described in Kato et al. (2011). CERES TOA irradiances and irradiance profiles computed using *CALIPSO*-, *CloudSat*-, and MODIS-derived cloud and aerosol properties are also included.

Uncertainties in radiative fluxes that account for sources of both random and systematic error are established through three independent methods: comparisons against surface radiation measurements; differences between the independently derived SRB, ISCCP-FD, 2B-FLXHR-lidar, and C3M datasets; and sensitivity studies. TOA flux estimates from ISCCP-FD and CERES are sensitive to changes in observing system and diurnal sampling, respectively, leading to uncertainties in continent-scale monthly mean TOA radiative fluxes of up to 5 W m^{-2} (Mayer and Haimberger 2012; Wild et al. 2013; Loeb et al. 2014). Loeb et al. (2009), for example, state that after removing global biases, uncertainties of up to 4.2 W m^{-2} (2σ) may remain in large-scale long-time mean net outgoing radiation based on extensive sensitivity studies. They further note that in the absence of bias correction, imbalances in CERES global annual mean net outgoing radiation are 6.5 W m^{-2}. Uncertainties of this magnitude significantly impact analysis of trends and variability but are not prohibitive for documenting the mean state.

At the surface, however, comparisons against the BSRN suggest that regional monthly mean errors in the current ISCCP-FD and SRB products can be much larger, approaching 10 W m^{-2} on the continental and ocean-basin scales examined here (Zhang et al. 2004). While random errors are significantly reduced when data are averaged to the large time and space scales addressed here, biases can result from systematic errors in the forward models and associated assumptions used in the component algorithms. Such errors, known as structural errors, impact all satellite datasets because of the computational costs of processing large volumes of data and the underconstrained nature of remote sensing problems. Since it is not generally possible to observe all of the parameters required to define complete physical models that map observed radiances onto the geophysical parameters of interest, less sophisticated forward models must be used and a subset of influence parameters must be specified that cannot be explicitly retrieved owing to the limited information content of the measurements (Rodgers 2000). The magnitude of the errors that results from these simplifications is often scene dependent, leading to regionally and seasonally varying biases that can lead to residual biases even upon aggregation to much larger scales (e.g., Berg et al. 2006).

Extensive previous research has documented the potential sources of structural errors in surface radiative flux estimates. Sensitivity studies in which all key algorithm inputs are perturbed by amounts consistent with their intrinsic uncertainties and reprocessing up to a year of flux calculations (billions of individual pixels) suggest that the dominant sources of structural errors in satellite-based estimates of surface shortwave fluxes are uncertainties in assumed cloud effective radii and aerosol optical properties. Uncertainties in surface air and skin temperatures and lower-tropospheric water vapor are found to dominate biases in surface longwave fluxes (L'Ecuyer and Stephens 2003; Zhang et al. 2004, 2006, 2007, 2010). The use of one-dimensional plane-parallel radiative transfer calculations to generate fluxes at the *CloudSat* resolution has also been shown to lead to systematic uncertainties in inhomogeneous cloud scenes (Barker et al. 1998). As a result the ISSCP-FD algorithm employs a correction for the effects of subgrid inhomogeneity based on the parameterization of Cairns et al. (2000). The plane-parallel approximation has, however, been shown to be more accurate for deriving domain-averaged broadband radiative fluxes than for narrowband radiances on smaller spatial scales (Benner et al. 2001; Ham et al. 2014).

Since the radiation datasets cover different spatial resolutions, use inputs from distinct sensors, adopt different background assumptions, employ different radiative transfer solvers, and have different diurnal sampling characteristics, the range of estimates from these products can be expected to provide a reasonable approximation of the aggregate effects of structural errors in each product. For example, each dataset can be expected to exhibit a unique sensitivity to three-dimensional effects owing to their distinct spatial resolutions, and any systematic errors that result from these effects will be manifested in the range of large-scale flux estimates derived from these products. To generate uncertainty estimates specific to the regions and time scales examined here, the range of flux estimates from the four datasets described above was assessed. In nearly all cases, the resulting uncertainty estimates capture the magnitude of the structural errors implied by previously published sensitivity studies with two exceptions. The standard deviations of regional DLR between the four datasets are slightly smaller than previous estimates of the errors that could result from uncertainties in lower-tropospheric humidity and, to a lesser extent, cloud liquid water path. Likewise, standard deviations of DSR were smaller than those estimated based on sensitivities to errors in assumed cloud liquid water path and effective radii. Uncertainties in DLR and DSR were therefore increased to represent possible regime-dependent errors resulting from these algorithm assumptions. On regional scales (see Table 2), fractional uncertainties are consistent with the RMS differences between satellite-based estimates and ground-based observations reported by Kato et al. (2012) and Kato et al. (2013). This suggests that the aggregate effects of structural errors in radiative flux products owing to the plane-parallel approximation or other algorithmic assumptions do not result in significant biases on the continental and monthly scales of interest to this study.

b. *Oceanic turbulent heat fluxes*

Turbulent heat fluxes (latent heat LE and sensible heat SH) over the ocean derive primarily from SeaFlux version 1.0. SeaFlux (Curry et al. 2004; Clayson et al. 2015, manuscript submitted to *Int. J. Climatol.*) estimates turbulent heat fluxes from the ocean surface by applying bulk formulas to atmospheric temperature and humidity provided by Special Sensor Microwave Imager (SSM/I) retrievals using a newly developed neural net algorithm (Roberts et al. 2010). A modified sea surface temperature dataset that specifically accounts for diurnal warming (Clayson and Bogdanoff 2013) is included to reduce both mean biases relative to in situ data and systematic errors at extremely low and high humidities. Air temperature retrievals using this method have shown the greatest increase in accuracy compared to other products, with biases now under 0.25°C on the monthly scales examined here across the spectrum of air–sea temperature differences. Winds are derived from the Cross-Calibrated Multi-Platform (CCMP) level-2.5 gridded swath product using a novel interpolation method based on temporal evolution in reanalyses [in this case the Modern-Era Retrospective Analysis for Research and Applications (MERRA)]. This model-based interpolation uses the time tendencies from a high-resolution model analysis but is driven through the satellite observations in a smooth manner. The resulting SeaFlux dataset is produced at a higher 0.25° spatial and 3-hourly temporal resolution than other satellite-based turbulent heat flux products. The version of the SeaFlux product used here covers the 1998–2007 time period and integrates the Colorado State University SSM/I calibrated brightness temperature dataset (C. Kummerow 2011, personal communication).

Previous efforts to quantify the uncertainties in satellite estimates of air–sea fluxes suggest that the dominant sources of biases are likely retrievals of near-surface air temperature and humidity, sampling biases, and the parameterization of exchange coefficients in bulk formulas (e.g., Gulev et al. 2007a,b; Clayson et al. 2015, manuscript submitted to *Int. J. Climatol*; and references therein). Despite the effort taken to calibrate the fluxes against in situ observations and correct for diurnal sampling effects and interpolation errors, systematic errors may remain in ocean turbulent heat flux estimates on larger time and space scales that can influence subsequent applications (e.g., Trenberth et al. 2001; Josey et al. 2014). Brunke et al. (2011), for example, compared ocean turbulent heat fluxes from 11 different global flux datasets to in situ observations from 12 cruises and found biases as large as 6 and 20 $\mathrm{W\,m^{-2}}$ in SH and LE fluxes, respectively. The uncertainties in SeaFlux fluxes adopted here are adapted based on the error propagation analyses reported in (Roberts et al. 2010; Clayson et al. 2015, manuscript submitted to *Int. J. Climatol.*). On global scales, LE and SH errors are found to be 14 and 6 $\mathrm{W\,m^{-2}}$, respectively, while those for individual basins are ~10% and ~25%.

TABLE 2. Contributions of individual continents and ocean basins to the annual mean energy flux into Earth's surface. Fluxes are reported in petawatts (10^{15} W) so that the values reported for individual regions reflect the partitioning of the global total (last row) between them (Fasullo and Trenberth 2008a). For conversion purposes, 1 W m^{-2} globally equates to 0.511 PW, while for global land 1 W m^{-2} = 0.147 PW and global oceans 1 W m^{-2} = 0.364 PW. The areas (in 10^{12} m^2) of all continents and basins as defined in Fig. 2 are provided for converting fluxes in individual regions. The full names of each term are provided in Table 3.

Map	Continent/basin	Area	*P*	LE	DLR	DSR	ULW	USW	SH
01	North America	24.03	1.35 ± 0.07	0.82 ± 0.07	6.95 ± 0.13	3.76 ± 0.17	8.27 ± 0.13	0.63 ± 0.09	0.66 ± 0.17
02	South America	17.73	2.31 ± 0.11	1.40 ± 0.08	6.66 ± 0.10	3.68 ± 0.15	7.71 ± 0.07	0.46 ± 0.06	0.96 ± 0.13
03	Eurasia	53.23	3.06 ± 0.18	1.77 ± 0.28	15.9 ± 0.44	8.70 ± 0.50	19.5 ± 0.73	1.79 ± 0.12	1.86 ± 0.38
04	Africa	29.90	1.66 ± 0.08	1.32 ± 0.11	10.9 ± 0.22	7.10 ± 0.31	13.8 ± 0.19	1.68 ± 0.06	1.87 ± 0.21
05	Australia	7.558	0.31 ± 0.02	0.24 ± 0.04	2.70 ± 0.07	1.77 ± 0.09	3.50 ± 0.11	0.34 ± 0.05	0.60 ± 0.06
06	Island continent	1.484	0.29 ± 0.02	0.13 ± 0.03	0.53 ± 0.02	0.25 ± 0.02	0.60 ± 0.03	0.02 ± 0.01	0.05 ± 0.02
07	Antarctica	12.70	0.18 ± 0.05	0.01 ± 0.01	1.76 ± 0.22	1.62 ± 0.13	2.18 ± 0.09	1.23 ± 0.13	−0.2 ± 0.09
08	Arctic Ocean	10.15	0.21 ± 0.11	0.10 ± 0.02	2.32 ± 0.07	0.99 ± 0.04	2.61 ± 0.03	0.48 ± 0.09	0.07 ± 0.03
09	Caribbean Sea	4.345	0.36 ± 0.04	0.55 ± 0.05	1.76 ± 0.03	1.06 ± 0.03	1.99 ± 0.01	0.05 ± 0.01	0.05 ± 0.02
10	Mediterranean Sea	2.602	0.12 ± 0.02	0.29 ± 0.04	0.90 ± 0.02	0.56 ± 0.03	1.09 ± 0.01	0.03 ± 0.01	0.06 ± 0.02
11	Black Sea	0.470	0.03 ± 0.01	0.03 ± 0.01	0.15 ± 0.01	0.08 ± 0.01	0.18 ± 0.01	0.00 ± 0.01	0.01 ± 0.01
12	North Pacific	81.77	9.02 ± 0.74	7.76 ± 0.69	31.3 ± 0.51	16.7 ± 0.47	35.1 ± 0.31	0.97 ± 0.09	1.22 ± 0.29
13	North Atlantic	43.38	3.54 ± 0.38	4.06 ± 0.33	15.6 ± 0.23	8.12 ± 0.27	17.7 ± 0.17	0.51 ± 0.04	0.80 ± 0.18
14	Indian Ocean	75.37	6.29 ± 0.65	7.20 ± 0.69	27.1 ± 0.38	14.5 ± 0.40	30.6 ± 0.23	0.94 ± 0.07	1.31 ± 0.31
15	South Pacific	99.93	8.13 ± 0.81	8.88 ± 0.76	35.6 ± 0.55	19.3 ± 0.36	40.4 ± 0.33	1.35 ± 0.09	1.64 ± 0.37
16	South Atlantic	46.51	2.83 ± 0.37	3.58 ± 0.28	15.7 ± 0.18	8.35 ± 0.28	17.8 ± 0.14	0.69 ± 0.08	0.81 ± 0.18
—	Continents	146.6	9.17 ± 0.51	5.69 ± 0.57	45.4 ± 1.16	26.8 ± 1.34	55.6 ± 1.30	6.16 ± 0.50	5.71 ± 1.03
—	Oceans	364.5	30.5 ± 3.09	32.4 ± 2.83	130. ± 1.93	69.8 ± 1.85	147. ± 1.20	5.03 ± 0.44	5.96 ± 1.36
—	Global	511.2	39.7 ± 3.59	38.1 ± 3.42	176. ± 3.09	96.6 ± 3.18	203. ± 2.50	11.1 ± 0.93	11.6 ± 2.39

c. *Terrestrial turbulent heat fluxes*

The terrestrial counterparts to the ocean turbulent heat fluxes [or evapotranspiration (ET), for consistency with the companion water cycle study] are much more difficult to estimate because ET is highly variable in space and time, and ground-based observations (weighing lysimeters and eddy covariance measurements) are sparse and may not be representative of the continental scales targeted in this study. Satellite retrieval algorithms, on the other hand, offer more desirable spatial sampling, but their accuracy is severely limited by the assumptions required and the sparseness of in situ observations available for calibration and validation. Physical and empirical models of land surface processes offer a third alternative, but their accuracy is again limited by the quality of the input data and simplifications inherent to numerical models (Rodell et al. 2004a). From these considerations and the lack of a clear consensus regarding superiority of any particular approach, the estimates of terrestrial turbulent heat fluxes and their uncertainties used here were obtained from the average and standard deviation of three independent model- and observation-based sources.

1) PRINCETON SATELLITE-BASED EVAPORATION

The Princeton terrestrial ET algorithm uses the Penman–Monteith approach (Monteith 1965) with all model inputs and forcings, with the exception of wind and surface pressure, derived from satellite remote sensing. Surface resistance (the resistance of vapor flow through the transpiring crop and evaporating soil surface) is adjusted and ecophysiological constraints are applied to account for changing environmental factors. Evaporation and sublimation over snow-covered regions are calculated using a modified Penman equation. Instantaneous latent and sensible heat fluxes computed at the time of satellite overpass are linearly scaled to the equivalent daily evapotranspiration using the computed evaporative fraction and the daytime net radiation. Nighttime evaporation is modeled as a constant fraction (10%) of daytime evaporation. Interception losses (evaporation from the vegetation canopy) are computed using a simple water budget model. More detail can be found in Vinukollu et al. (2011). Both input meteorology and latent and sensible heat outputs have been extensively evaluated against eddy covariance tower data across the United States at the site scale on a monthly mean basis. Multiyear means are then compared against climatological evapotranspiration estimates over 26 major river basins, and zonal means are evaluated on an annual basis. Good correlations are found with in situ data, and the dataset is found to capture both seasonal cycles and major drought events.

2) MERRA

The NASA/GMAO MERRA reanalysis assimilates conventional in situ observations, satellite radiances, and several remotely sensed retrieved datasets over the duration of the Earth-observing satellite era (1979–present) (Rienecker et al. 2008, 2011). MERRA water and energy budget data are reported hourly on a nominal 0.5° × 0.67° grid, taking special care to report all relevant budget terms so that closure can be achieved. Like all reanalyses, analyzed perturbations of the model state variables exert significant influence on the physics budgets (Roads et al. 2002), which leads to imbalances in the physical terms of the budget. In MERRA, this influence is computed from the data assimilation and provided as a tendency term (called the analysis increment) in the budget equation that is used here to correct turbulent heat fluxes using regression equations based on Bosilovich and Schubert (2001). The quality of the MERRA global water and energy budgets is discussed in detail in Bosilovich et al. (2011). Trenberth et al. (2011) caution that the quality of the MERRA reanalysis changes over time and, specifically, that the MERRA ET exhibits large fluctuations associated with observing system changes, although these are likely to be more critical for trend analyses.

3) GLDAS

The Global Land Data Assimilation System (GLDAS) Rodell et al. (2004b) is a quasi-operational implementation of the land information system software (Kumar et al. 2006) that generates estimates of soil moisture, temperature, evapotranspiration, and runoff (among other parameters) by integrating satellite- and ground-based observational data products within a suite of land surface models (LSMs). The GLDAS ET estimates used here derive from the mean and standard deviation of 1.0°-resolution output from a four-member ensemble that included the Noah (Chen et al. 1996; Ek et al. 2003; Koren et al. 1999), Community Land Model (CLM) version 2 (Bonan 1998), Variable Infiltration Capacity (VIC) (Liang et al. 1994), and Mosaic (Koster and Suarez 1996) LSMs. Each model was forced with a combination of meteorological fields (air temperature, humidity, wind speed, and surface pressure) from the National Centers for Environmental Prediction (NCEP) Global Data Assimilation System product, 3-hourly precipitation fields from a downscaled version of the Global Precipitation Climatology Project (GPCP) one-degree daily (1DD) product version 1.1 (Huffman et al. 2001), and downward shortwave and longwave radiation fields from the Air Force Weather Agency (AFWA) cloud analyses using the schemes of Shapiro (1987), Idso (1981), and Wachtmann (1975). Land cover data from the University of Maryland (Hansen et al. 2000), soils data from Reynolds et al. (2000), and the GTOPO30 digital elevation model were used to parameterize the land surface in all models. The GLDAS simulations were spun up from 1979, and multiyear means were computed for each month by averaging the four models over the period 1998–2008. Inland water bodies (e.g., the Great Lakes) and ice sheets (Greenland and Antarctica) not modeled by GLDAS were filled with MERRA data in order to conform to the continental delineation defined for this study.

The resulting standard deviations in annual mean ET fluxes on continental scales are among the largest of any class of fluxes in this study, ranging from 10% to 20%. These results are consistent with the spread in multiyear global mean land ET estimates between the models examined in Mueller et al. (2011) but somewhat smaller than those reported in Jimenez et al. (2011). The latter reports ranges of up to 40% attributed to differences in methodology and the choice of both formulation and forcing datasets, although their estimates are based on the maximum and minimum estimates from a larger number of ET datasets as opposed to the standard deviations reported here. Jimenez et al. (2011) further note that, like the precipitation datasets described below, the magnitude of the absolute differences between ET estimates is proportional to the mean magnitude of the ET flux itself, and thus regions characterized by higher evaporation contribute more to the overall uncertainty than drier regions.

d. Atmospheric latent heat release

Global precipitation observations offer an independent constraint on nonradiative heat transfer from the surface to the atmosphere and provide an additional pathway for coupling the energy and water cycles in the optimization procedure described below. While detailed accounting of specific microphysical processes is required for deriving vertical profiles of latent heating, the total condensate removed from the atmosphere in the form of precipitation provides a tight constraint on the column-integrated latent heat release on the large time and space scales considered here (Tao et al. 1993). The GPCP monthly satellite gauge precipitation analysis (Adler et al. 2003; Huffman et al. 2009), version 2.2, is adopted as the exclusive dataset to derive atmospheric latent heating in this study.

The multisatellite merged GPCP dataset provides global, monthly estimates of surface precipitation at 2.5° resolution from 1979 to present though this study made use of the period January 2001 to December 2010, the most recent 10-yr period available at the time the analysis began. The core monthly GPCP merged product employs precipitation estimates from the 0600 and 1800 LT low-orbit satellite SSM/I and Special Sensor Microwave Imager/ Sounder (SSMIS) microwave data to perform a monthly, regional calibration of geosynchronous-orbit satellite infrared (IR) data in the latitude band 40°N–40°S. At higher latitudes the SSM/I and SSMIS microwave estimates are combined with estimates based on TOVS or AIRS. A bias adjustment of satellite estimates using gauges over land is conducted to mitigate reduced sensitivity of passive microwave observations over more emissive land surfaces. The absolute magnitudes are, therefore, considered reliable and interannual changes are robust. Because of the inhomogeneous nature of the satellite information included in the dataset and the inclusion of information from somewhat lower-quality microwave sensors/algorithms to improve temporal coverage, trends and other small signals should be interpreted cautiously.

The monthly GPCP dataset includes fields of random error estimates, which were used to develop 10-yr climatological errors for this analysis. These error estimates are consistent with the uncertainty estimates derived from the intercomparison of several satellite rainfall datasets by Adler et al. (2012). Other studies comparing independent precipitation estimates from active and passive sensors support the assertion that structural errors due to sensitivity to light rain and frozen precipitation, algorithm assumptions, and sampling are not likely to exceed these estimates on the scales of interest to this study (Berg et al. 2006, 2010; Behrangi et al. 2014). Precipitation from heavy events and in mountainous areas may, however, be underestimated, although GPCP version 2.2 is improved in this regard over previous versions (Adler et al. 2012).

e. *Additional constraints*

This study also indirectly leverages a number of additional datasets related to components of the water cycle. New estimates of continental runoff Q from a combination of near-coast gauging stations and modeling (Clark et al. 2015), total precipitable water vapor from AIRS (Susskind et al. 2011), atmospheric convergence C from MERRA and two water vapor transport datasets (Liu et al. 2006; Hilburn 2009), and estimated changes in terrestrial water storage dS from the Gravity Recovery and Climate Experiment (GRACE) (Swenson and Wahr 2002; Landerer and Swenson 2012). Since these quantities enter the analysis peripherally through the physical coupling of the energy and water cycles introduced by the optimization approach described in section 4, they are not discussed in detail here. The interested reader is directed to the companion study by Rodell et al. (2015) for a more complete discussion of the methodologies and uncertainties in these datasets.

3. The observed global energy budget at the start of the twenty-first century

The unadjusted annual mean global energy budget for the first decade of the twenty-first century obtained using the datasets described above is presented in Fig. 1. TOA radiative fluxes are consistent with those reported in other recent efforts to document the global energy budget. Solar insolation of 340 W m^{-2} is balanced by 102 W m^{-2} of outgoing shortwave radiation (OSR) and 238 W m^{-2} of outgoing longwave radiation (OLR) yielding a planetary albedo of 0.3 ± 0.012 and a global emitting temperature of 254.5 ± 0.5 K. For historical perspective, these values agree very well with the early estimates from *Nimbus-3* observations reported more than four decades ago by Vonder Haar et al. (1972) (0.29 and 254 K), though the present estimates are likely considerably more precise.

Energy fluxes between the atmosphere and surface, on the other hand, differ from those reported in other recent global energy budget reconstructions since no surface or atmospheric energy balance constraints have been applied. Notably, DLR and DSR are 11 and 7 W m^{-2} higher than those reported by Trenberth et al. (2009), while latent heating is 13 W m^{-2} lower than that reported by Stephens et al. (2012b) and 10 W m^{-2} lower than in Wild et al. (2013). Figure 1 indicates that our current best estimates of downwelling radiation at the surface and atmospheric radiative flux divergence exceed turbulent heat transfer from the surface to the atmosphere by 16 and 12 W m^{-2}, respectively, on the annual average. Comparison of energy budgets derived using all possible combinations of the alternative datasets listed above (not shown) suggest that these imbalances are not unique to the specific choice of datasets adopted here. Global annual mean surface energy imbalances, for example, range from 13 to 24 W m^{-2} for the range of datasets examined here, reflecting uncertainties in the component flux estimates.

As noted above, extensive research has been conducted to assess potential sources of structural error that may be responsible for biases in satellite-based estimates of each of the fluxes depicted in Fig. 1. Uncertainty in atmospheric and cloud properties can have significant impacts on computed downwelling fluxes at the surface that can lead to biases of up to 4 and 7 W m^{-2} in DSR and DLR, respectively (Kato et al. 2013) (within the error bars reported on Fig. 1). Similarly, the recent studies of Adler et al. (2012) and Behrangi et al. (2014) suggest that biases in the latest global precipitation datasets may be as large as 9% (or 7 W m^{-2}), consistent with earlier studies that indicated that systematic errors of this magnitude may result from regime-dependent variations in liquid water path thresholds for identifying rainfall, raindrop size distributions, the partitioning of cloud and rainwater, and column-integrated water vapor (Berg et al. 2002, 2006).

Likewise, Brunke et al. (2011) and Clayson et al. (2015, manuscript submitted to *Int. J. Climatol.*) note

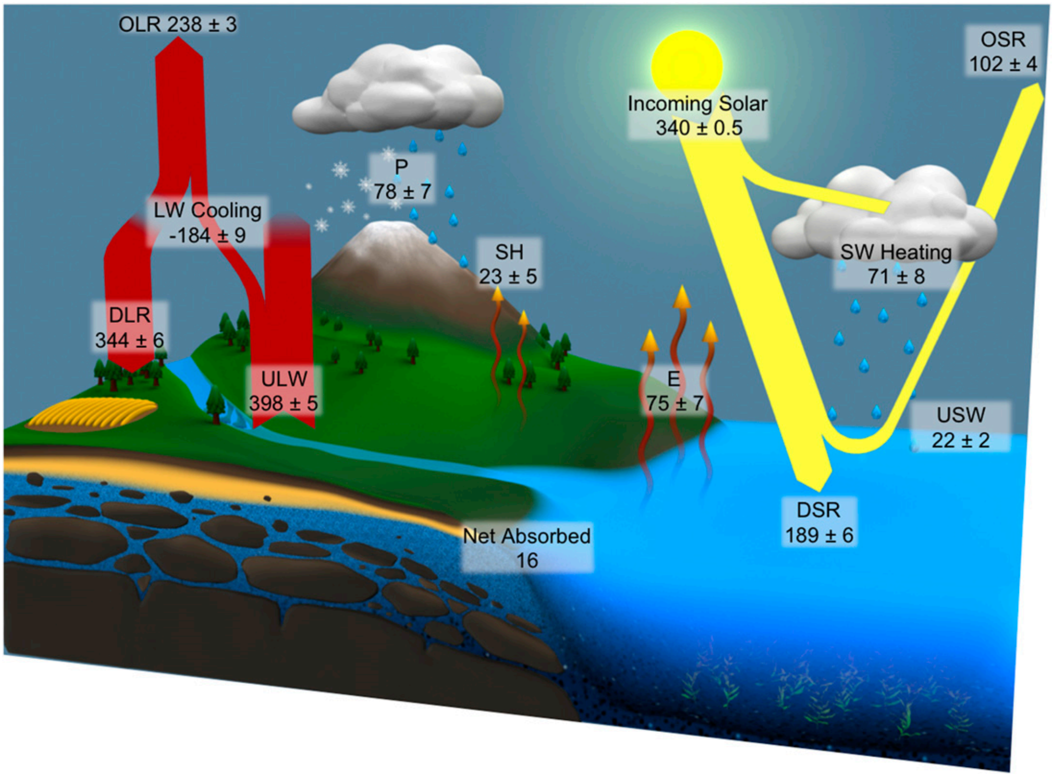

FIG. 1. The observed annual mean global energy budget of Earth over the period 2000–09 (fluxes in W m^{-2}). Note that each flux value corresponds to the aggregate from all surfaces around the globe. Longwave and shortwave fluxes are plotted over land and ocean regions, respectively, merely for convenience. The small fraction of DLR that is reflected by Earth's surface has been absorbed into the ULW.

that the bulk formulas at the root of the SeaFlux ocean turbulent heat flux estimates are sensitive to the choice of exchange coefficients, errors in satellite retrievals, and the interpolation methodology. While care has been taken to calibrate the SeaFlux algorithm against in situ observations, systematic errors may be as large as 6 and 14 W m^{-2} in sensible and latent heat fluxes, respectively, owing primarily to uncertainty in satellite retrievals of near-surface air temperature and humidity (Brunke et al. 2011; Clayson and Bogdanoff 2013; Clayson et al. 2015, manuscript submitted to *Int. J. Climatol.*). In addition, the intercomparisons of observational estimates of evaporative and sensible heat fluxes over land by Jimenez et al. (2011) suggest structural biases between datasets that vary systematically with surface type and season, potentially leading to even larger biases on the monthly and regional scales examined below.

Continental and basin scales

Given the importance of the partitioning of energy between the atmosphere and surface and the fact that the largest energy imbalances are found at the surface, it is important to seek the source of these imbalances. A summary of the contributions of individual continents and ocean basins to the global mean surface energy balance is presented in Fig. 2. Surface radiative fluxes have been combined into a net surface radiative flux for brevity ($F_{\mathrm{NET}} = \mathrm{DLR} + \mathrm{DSR} - \mathrm{ULW} - \mathrm{USW}$). Estimated uncertainties in each of these parameters, expressed as a 1σ deviation about the mean value, are presented in Fig. 3 for comparison.

Surprisingly, while satellite observations generally have higher information contents over the oceans, these regions tend to exhibit the largest energy imbalances. Uncertainties in net radiation into the oceans, for example, are ~10 W m^{-2} owing, in part, to much smaller variability of dark ocean albedo and the smaller diurnal cycle of ocean temperatures relative to many land regions. Uncertainties in latent heating estimates tend to be larger over oceans than over land because of larger evaporation, but this is at least partially offset by much smaller uncertainties in ocean sensible heat transfer. When combined, this results in smaller flux uncertainties over ocean basins than over land, yet the energy imbalances in Fig. 2 are clearly larger over oceans than over land.

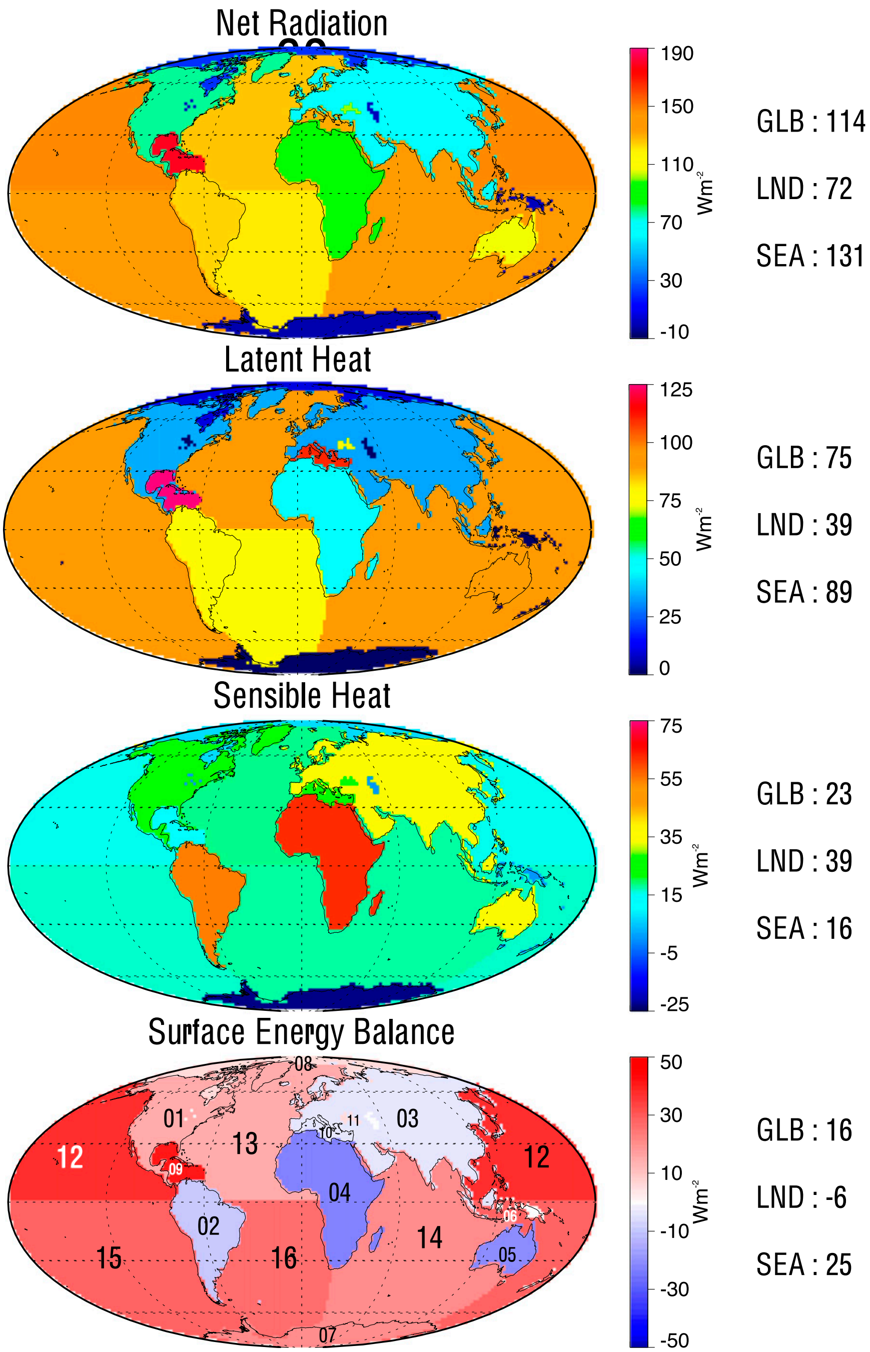

FIG. 2. Annual mean surface energy fluxes for each of the seven continents and nine ocean basins adopted in this study. (a) Net downwelling surface radiation (downwelling minus upwelling LW + SW radiation). (b),(c) Latent and sensible turbulent heat fluxes. (d) The resulting net surface energy imbalances defined as the difference between radiation and the two turbulent heat fluxes. Corresponding global (GLB), continental (LND), and ocean-basin (SEA) means are summarized on the right side of the figure (in W m^{-2}). The numerical labels on each continent and basin in (d) reference the identifiers used in Tables 2 and 4.

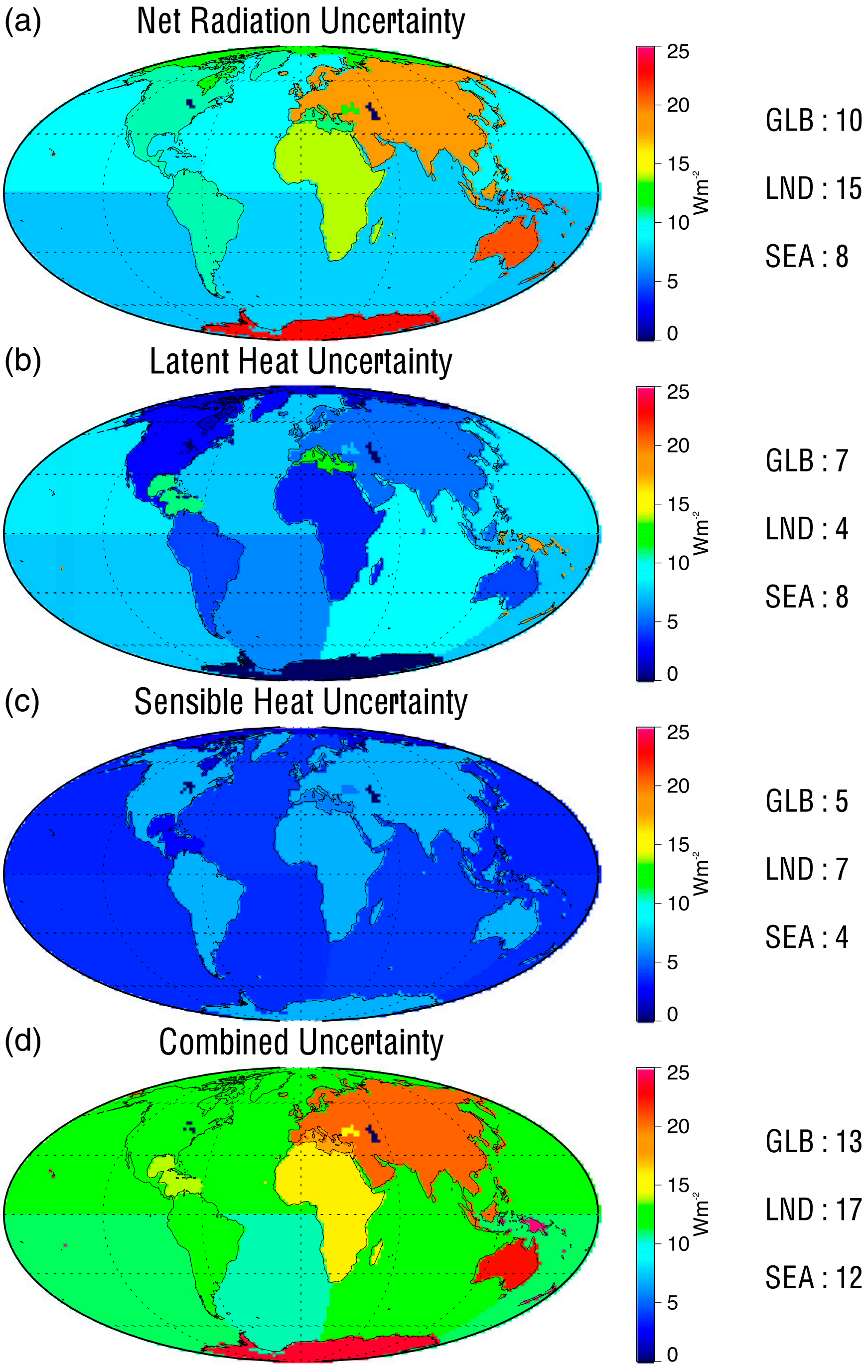

FIG. 3. Estimated uncertainties in observed annual mean surface (a) radiative fluxes, (b) sensible heat fluxes, and (c) latent heat fluxes for all major continents and ocean basins. (d) The uncertainty in net surface–atmosphere energy exchange is computed assuming that the errors in the component fluxes are independent [i.e., $\delta(x_1 + x_2 + \cdots + x_N) = \sqrt{\sum_{i=1}^{N} \delta x_i^2}$].

The apparent contradiction between Figs. 2 and 3 may be partially explained by differences in the way turbulent heat fluxes are derived over land relative to over oceans. Satellite-based land flux algorithms like the Princeton ET approach directly incorporate closure constraints and ingest surface radiative fluxes, while the SeaFlux turbulent heat fluxes are derived independent of surface radiation with the exception of a diurnal cycle correction based on diurnal variations in solar insolation. Thus, despite the large structural biases that can be introduced in land ET datasets from specific choices of formation and forcing datasets (Jimenez et al. 2011), closure is more readily achieved provided that consistent datasets are used. Imbalances between downwelling radiation and latent heating over ocean basins are, therefore, the primary driver of global surface energy imbalances; the integrated surface energy budget over land produces an imbalance of just $-6\,\mathrm{W\,m^{-2}}$, while integrating all ocean basins results in an imbalance of $25\,\mathrm{W\,m^{-2}}$.

By comparison, analysis of data collected by the Argo array since 2005 suggests that ocean heat content (OHC) has changed by $\sim 0.6 \pm 0.4\,\mathrm{W\,m^{-2}}$ (Willis et al. 2009; Lyman et al. 2010). Despite the large fractional uncertainties in these estimates owing to challenges in sampling the Arctic, marginal seas, and depths below 2000 m (Trenberth et al. 2014), they constrain the net heat absorbed into the oceans to be at least an order of magnitude smaller than the imbalances implied by combining the component fluxes. Also, with the exception of the Antarctic circumpolar current that is not responsible for significant heat transport, all of the major wind-driven gyres lie entirely within individual basins, so it is unlikely that heat transport between basins by deep ocean circulations can account for such large imbalances. Furthermore, achieving balance through heat transport would require compensating positive and negative imbalances in adjacent basins, yet Fig. 2 suggests that the imbalances are of the same sign in all ocean basins.

A closer look at Figs. 2d and 3d also suggests that the magnitude of the imbalances in a number of the ocean basins (e.g., the South Atlantic) exceeds the combined uncertainty in the component fluxes. Recall, however, that the uncertainties reported represent one-standard-deviation error bars on each component flux. Imbalances that exceed the reported uncertainties may, therefore, be explained by errors greater than one standard deviation in one or more component fluxes. A closer look at the uncertainties in all component fluxes compiled in Table 2 reveals that the net surface energy imbalance of $28\,\mathrm{W\,m^{-2}}$ in the South Atlantic could be nearly eliminated if DLR and DSR are reduced by their 1σ uncertainties while emitted longwave flux (ULW), reflected shortwave flux (USW), Q_s, and LE are increased by theirs. While it seems unlikely that estimates of downwelling and upwelling fluxes would be biased in precisely this manner, this example illustrates that balance can, in principle, be achieved within the stated uncertainties of the component fluxes. This concept is explored quantitatively in the next section through the use of a general framework for adjusting component fluxes subject to relevant balance constraints.

4. Objectively imposing balance constraints

The presence of large surface energy imbalances over the oceans highlights the challenge of integrating independent datasets into a more complete budget. While it is desirable to maintain independent algorithms for each of the component fluxes for practical reasons and to avoid unwanted correlations that may influence subsequent analyses, global and regional energy budget and water cycle closure relationships provide valuable information that is neglected when component fluxes are derived in isolation. Since closure arguments do not apply on the scales of instantaneous satellite fields of view from which the individual fluxes are derived (especially over oceans), it is not possible to invoke such constraints on individual retrievals, but they may be applied a posteriori to averages over larger time and space scales. Motivated by a desire to generate a balanced energy budget subject to all available constraints, including the latest in situ estimates of changes in ocean heat content, we propose a new objective approach for adjusting all component fluxes that explicitly accounts for the relative accuracy to which they are known. The method is sufficiently general that it can simultaneously include both energy and water balance constraints to take advantage of the coupling introduced through latent heating.

There are several different approaches for solving an optimization problem of this type. Adapting concepts from the variational data assimilation and optimal estimation retrieval communities, the method adopted here seeks to recast the problem into a form that minimizes a cost function subject to a prescribed set of constraints. In general, any energy or water balance constraint can be written in the form

$$R = \sum_{i=1}^{M} F_i - \sum_{o=1}^{N} F_o, \tag{1}$$

where F_i and F_o represent all fluxes into and out of the system, respectively, and the residual R represents the net storage in the system. The goal is to find the most likely vector of fluxes $\mathbf{F} = (F_i, F_o)$ given the vector of independent observational flux datasets $\mathbf{F}_{\mathrm{obs}} = (F_{i,\mathrm{obs}}, F_{o,\mathrm{obs}})$ and the observed value of the residual R_{obs}. At Earth's surface, for example, downwelling longwave and shortwave radiation (F_i) are balanced by reflected shortwave radiation, emitted longwave radiation, and fluxes of latent and sensible heat from the surface to the atmosphere (F_o) to within a very small residual. Recent analysis of OHC from the Argo array suggests that the residual ocean heat storage R_{obs} is on the order of $0.6 \pm 0.4\,\mathrm{W\,m^{-2}}$. Changes in OHC account for about 90% of the global annual mean heat storage, so other contributions, such as those from land heat storage and melting glaciers, are assumed to fall within the uncertainties adopted for this constraint (Trenberth et al. 2014). Given the narrow range of surface imbalances allowed by the OHC constraint (0.2–1 W m^{-2}) relative to the errors in the component fluxes (several W m^{-2}), obtaining the optimal **F** requires adjusting each of the component fluxes within their respective error bounds in such a way as to reduce the implied storage to lie within the error bars on R_{obs}.

This is achieved by invoking two common (and necessary) assumptions concerning the uncertainties in the component fluxes: that they are random and Gaussian. While it is difficult to justify either of these assumptions, they are required in the absence of definitive bias or error distribution information. Under these assumptions, optimal flux values will maximize the joint probability:

$$P(\mathbf{F}\,|\,\mathbf{F}_{\mathrm{obs}}, R_{\mathrm{obs}}) = \exp[-(\mathbf{F}-\mathbf{F}_{\mathrm{obs}})^{\mathrm{T}}\mathbf{S}_{\mathrm{obs}}^{-1}(\mathbf{F}-\mathbf{F}_{\mathrm{obs}})] \times \exp\left[-\frac{(R-R_{\mathrm{obs}})^2}{\sigma_R^2}\right], \tag{2}$$

where the distinction between the incoming and outgoing fluxes has been dropped for simplicity. The term $\mathbf{S}_{\mathrm{obs}}$ is the error covariance of all fluxes derived from the uncertainty analyses described above, and σ_R^2 is the error variance in the heat storage constraint. The maximum occurs when the following cost function is a minimum:

$$J = (\mathbf{F}-\mathbf{F}_{\mathrm{obs}})^{\mathrm{T}}\mathbf{S}_{\mathrm{obs}}^{-1}(\mathbf{F}-\mathbf{F}_{\mathrm{obs}}) + \frac{(R-R_{\mathrm{obs}})^2}{\sigma_R^2}. \tag{3}$$

Since the residual R is just a linear combination of the component fluxes, the cost function is quadratic and can be minimized exactly by setting the derivative with respect to **F** equal to 0. Optimal values of the component fluxes are given by

$$\mathbf{F} = \mathbf{F}_{\mathrm{obs}} + \mathbf{S}_F\mathbf{K}^{\mathrm{T}}\mathbf{S}_{\mathrm{obs}}^{-1}(R_{\mathrm{obs}} - \mathbf{K}\mathbf{F}_{\mathrm{obs}}), \tag{4}$$

where $\mathbf{K}$ is the Jacobian of R with respect to the component fluxes and $\mathbf{S}_F = (\mathbf{K}^{\mathrm{T}}\mathbf{S}_y^{-1}\mathbf{K} + \mathbf{S}_{\mathrm{obs}}^{-1})^{-1}$ is the error covariance for the component fluxes after optimization. If Gaussian statistics are assumed, Eq. (4) represents both the most probable posterior estimate and minimum variance estimate of the parameters of interest subject to the constraint imposed by the residual or storage R (L'Ecuyer and Stephens 2002). As a metric for establishing the quality of the final fit, one can apply the χ^2 test to the results. To the extent that errors are random and Gaussian, a value of the quantity

$$\chi^2 = (\mathbf{F}-\mathbf{F}_{\mathrm{obs}})^{\mathrm{T}}\mathbf{S}_{\mathrm{obs}}^{-1}(\mathbf{F}-\mathbf{F}_{\mathrm{obs}}) + \frac{(R-R_{\mathrm{obs}})^2}{\sigma_R^2} \tag{5}$$

that is less than or equal to the number of degrees of freedom in the system (i.e., the total number of individual fluxes being optimized) indicates that the resulting flux adjustments do not drastically violate the error assumptions. A larger value of χ^2 is indicative of larger than anticipated biases in one or more of the component fluxes. Another simple (but valuable) metric of the success of the optimization is a direct comparison of the magnitudes of the adjustments made to each component flux against their estimated uncertainties. Energy budget residuals, computed as the sum of the adjustments to the component fluxes, that exceed associated error bounds are indicative of areas where balance could not be adequately achieved.

One of the principal advantages of this approach lies in the fact that it can be scaled to arbitrarily complex problems involving any number of fluxes and constraints. In particular, it can be used to establish an explicit link between the energy budget and water cycle through the connection between latent heating, evaporation, and precipitation. In this way, disparate observational datasets that are seldom considered together, such as radiative fluxes and surface runoff, can be coupled to their mutual benefit through their relationships to precipitation and evaporation in energy and water budget closure equations. This simultaneous accounting of both energy and water cycles is a unique aspect of this study and the companion water cycle paper that allows twice as many closure constraints to be leveraged to provide an internally consistent set of estimates of energy and water fluxes representative of the climate in the first decade of the twenty-first century.

a. *Application to energy and water budgets*

This method for imposing closure constraints on independent observational flux datasets has been applied to annual and monthly mean energy and water fluxes on global and continental scales by adopting closure constraints appropriate to each specific time and space scale. Over land surfaces, annual mean energy and water cycle closure require (in energy units)

$$L_v(dS_{\mathrm{co},i} = P_{\mathrm{co},i} - \mathrm{LE}_{\mathrm{co},i} - Q_{\mathrm{co},i}) \quad \text{and} \tag{6}$$

$$\mathrm{NET}_{\mathrm{co},i} = \mathrm{DLR}_{\mathrm{co},i} + \mathrm{DSR}_{\mathrm{co},i} - \mathrm{ULW}_{\mathrm{co},i} - \mathrm{USW}_{\mathrm{co},i} - \mathrm{SH}_{\mathrm{co},i} - L_v\mathrm{LE}_{\mathrm{co},i}\,, \tag{7}$$

where dS is the change in surface water storage and NET represents energy absorbed at the surface. All other fluxes are as defined in Table 3, and the latent heat of vaporization L_v is taken to be 2500 kJ kg^{-1} (2800 kJ kg^{-1} for sublimation over ice surfaces). Similarly, in the atmosphere we require

TABLE 3. Observed components of the global and annually averaged energy budget and their uncertainties before and after optimization. All values are reported in energy flux units (W m^{-2}). The reader is referred to the companion water cycle paper (Rodell et al. 2015) for additional details regarding runoff, atmospheric convergence, and water storage datasets used in the water budget closure equations.

Full Name	Abbreviation	Original	Constrained
Incoming solar	F	340.2 ± 0.1	340.2 ± 0.1
Outgoing shortwave	OSR	102 ± 4	102 ± 2
Outgoing longwave	OLR	238 ± 3	238 ± 2
Downwelling LW at surface	DLR	344 ± 6	341 ± 5
Downwelling SW at surface	DSR	189 ± 6	186 ± 5
Surface emitted	ULW	398 ± 5	399 ± 4
Surface reflected	USW	22 ± 2	22 ± 2
Sensible heat	SH	23 ± 5	25 ± 4
Atmospheric latent heat (precipitation)	P	78 ± 7	81 ± 4
Surface latent heat (evaporation)	LE	75 ± 7	81 ± 4
Atmospheric convergence	C	−0.6 ± 4	0 ± 1
Surface runoff (derived)	Q	3	0
Atmospheric water storage (derived)	dW	−4	0
Surface water storage (derived)	dS	3	0
Surface NET (derived)	NET	−16	0.45
Atmospheric NET (derived)	NETA	14	0

$$L_v(dW_{\text{co},i} = C_{\text{co},i} - P_{\text{co},i} - \text{LE}_{\text{co},i}) \quad \text{and} \tag{8}$$

$$\begin{aligned}\text{NETA}_{\text{co},i} = F_{\text{co},i} &- \text{OLR}_{\text{co},i} - \text{OSR}_{\text{co},i} - \text{DLR}_{\text{co},i} \\ &- \text{DSR}_{\text{co},i} + \text{ULW}_{\text{co},i} + \text{USW}_{\text{co},i} \\ &+ \text{SH}_{\text{co},i} + L_v P_{\text{co},i} + \text{CS}_{\text{co},i},\end{aligned} \tag{9}$$

where dW is the change in total precipitable water in the atmospheric column, NETA represents atmospheric heat storage, C denotes atmospheric moisture convergence, and CS is the atmospheric convergence of dry static energy and kinetic energy. These equations apply to all continents i on annual or monthly scales and explicitly demonstrate how fluxes of energy and water are coupled through the latent heat release. Similar equations apply to each ocean basin with one important distinction: an additional term must be added to each of the surface budget equations [Eqs. (6) and (7)] to account for water and heat transports between basins that occur on all time and space scales.

On global scales, mass continuity and water balance also require

$$L_v(dS_L + dS_O = dW_L + dW_O), \tag{10}$$

$$L_v(C_L = -C_O), \tag{11}$$

$$Q_L = -Q_O, \tag{12}$$

$$\text{OT}_O = 0, \quad \text{and} \tag{13}$$

$$\text{CS}_L = -\text{CS}_O, \tag{14}$$

where the subscripts L and O correspond to the sum over all land regions and ocean regions, respectively. The term OT_O is the net oceanic transport (of heat or water) integrated over all ocean basins.

To account for the additional complications of storage and transport on monthly scales, the optimization is executed in stages. First, all annual fluxes are simultaneously optimized by minimizing a large matrix of cost functions analogous to Eq. (3) derived from applying Eqs. (6)–(14) to all seven individual continents and the sum of all ocean regions on annual scales. The terms $dS_{\text{co},i}$, dS_O, $dW_{\text{co},i}$, and dW_O are assumed to vanish on the annual mean, while estimates of all other terms derive from the datasets described in section 2. It is further assumed that $\text{NET}_{\text{co},i}$, $\text{NETA}_{\text{co},i}$, and all of the NETA_O are small on annual scales since most of the excess energy in today's climate is absorbed into the oceans (Trenberth et al. 2014). This assumption ignores trends in terrestrial storage evident in GRACE observations. Greenland, Antarctica, and the glaciers along the Gulf of Alaska, in particular, have been shedding ice at a total rate of 380 $\text{km}^3\,\text{yr}^{-1}$ (Luthcke et al. 2013), but here, dS is derived from detrended time series, and mean continental water budgets are assumed with annual dS equal to zero. There has also been recent evidence of trends in atmospheric water vapor (e.g., Chung et al. 2014), but the implied energy fluxes are at least an order of magnitude less than those inferred from observed changes in OHC; thus it is assumed that only the small residual flux of energy into the oceans needs to be considered on these scales. To reduce the impact of any biases these assumptions may introduce, uncertainties in annual-mean dS and dW are inflated to be 0.2 W m^{-2} to encompass the possibility of residual terrestrial and atmospheric water storage.

Application of closure relations in oceanic regions is complicated by heat exchanges between basins. While observations of ocean heat transport exist (e.g., Trenberth and Fasullo 2008), we have chosen to treat the sum of all oceanic regions simultaneously by applying the closure relations in Eqs. (10)–(14) to the integrated ocean energy budget. The net oceanic flux adjustment is then partitioned among the individual basins using a Lagrange multiplier approach that inversely weights changes according to the error variances of the individual monthly estimates. Energy balance closure on monthly scales is also complicated by heat transport and storage. Lacking accurate global observations of these quantities, energy balance constraints are not applied directly on monthly scales. Instead, monthly best-guess fluxes are defined such that they match the sum to the optimized annual mean fluxes through incremental adjustments that are inversely proportional to their best-guess uncertainties. Again, a Lagrange multiplier approach is used to partition the residual between the adjusted annual mean and the sum of the unadjusted monthly mean fluxes among the individual months. Additional details concerning this approach and a complete discussion of the resulting water cycle estimates can be found in the companion manuscript by Rodell et al. (2015).

b. *Constrained global energy budget*

Application of Eq. (4) assuming a surface energy residual consistent with published estimates of OHC changes, neglecting heat storage over land regions (Trenberth et al. 2014), and noting that atmospheric convergence and runoff vanish on global scales yields the estimates of the surface energy budget and water cycle reported in the right-hand column of Table 3. While the resulting fluxes vary slightly if alternate datasets are adopted in the minimization, eight different variants tested all yield budgets within the quoted error bars, and the signs of the implied adjustments were found to be insensitive to the specific choice of flux datasets used. As should be expected almost all fluxes are adjusted through the optimization process, with the largest changes in parameters that are the least well constrained by observations (e.g., evaporation and DLR).

It is encouraging that the resulting flux estimates lie within the ranges implied by the uncertainties in the observed fluxes. The magnitudes of the adjustments are also generally consistent with published estimates of the uncertainties in each component flux. The precipitation adjustment, for example, falls within the uncertainty estimates provided by Adler et al. (2012), while adjustments to DLR are consistent with the findings of Stephens et al. (2012a). Furthermore, $\chi^2 = 1.9$, suggesting that the resulting ensemble of fluxes is consistent with assumed errors given that this problem is characterized by 9 degrees of freedom.

The error bounds on all fluxes are also reduced in the optimization process, but it must be emphasized these no longer represent the accuracy of the observations and should not be viewed as uncertainties in the traditional sense. Instead, they represent improved confidence in the overall ensemble of fluxes owing to the addition of balance constraints that are known to a much higher degree of confidence than the original observations but were not previously included in the independent algorithms. The error estimates associated with the unadjusted fluxes should be adopted when quoting uncertainties in individual flux datasets. The reduced error bounds also reflect the assumption that the uncertainties in the component fluxes are random and Gaussian. As noted already, this is not the case since several potential sources of structural error have been documented in the literature. Quantitative information concerning biases in component fluxes due to structural errors can easily be incorporated into the analysis by modifying the initial flux estimates, but more work is needed before such quantitative bias corrections are available. It is more likely, however, that such definitive bias information will be incorporated at the algorithm development level before reaching the stage where products are combined into a global budget.

The optimized estimates of global energy fluxes produced here (Fig. 4) represent a compromise between recently published energy budgets. Precipitation and evaporation, for example, are very similar to those reported by Trenberth et al. (2009), while sensible heating and DSR are in closer agreement with Stephens et al. (2012b). Overall, however, the values agree most closely with the surface-based analysis of Wild et al. (2013), with no differences exceeding 4 $\mathrm{W\,m^{-2}}$. The current satellite-based SH flux estimates are, however, larger than those reported elsewhere, exceeding estimates from reanalyses and models by as much as 30% (Trenberth et al. 2009; Wild et al. 2015). The estimates of DLR in both the present study and Wild et al. (2013) fall between the estimates from the other two reconstructions but agree very well with the value of 342 ± 3 $\mathrm{W\,m^{-2}}$ that was recently derived from surface observations by Wang and Dickinson (2013), although the uncertainty estimate provided in Fig. 4 is somewhat larger.

c. *Continental and basin scales*

The distribution of annual mean surface energy fluxes for all continents and ocean basins after imposing balance constraints is presented in Fig. 5. A complete summary of all component fluxes and corresponding uncertainties after optimization is compiled in Table 4 for reference. In general, the net radiation incident on

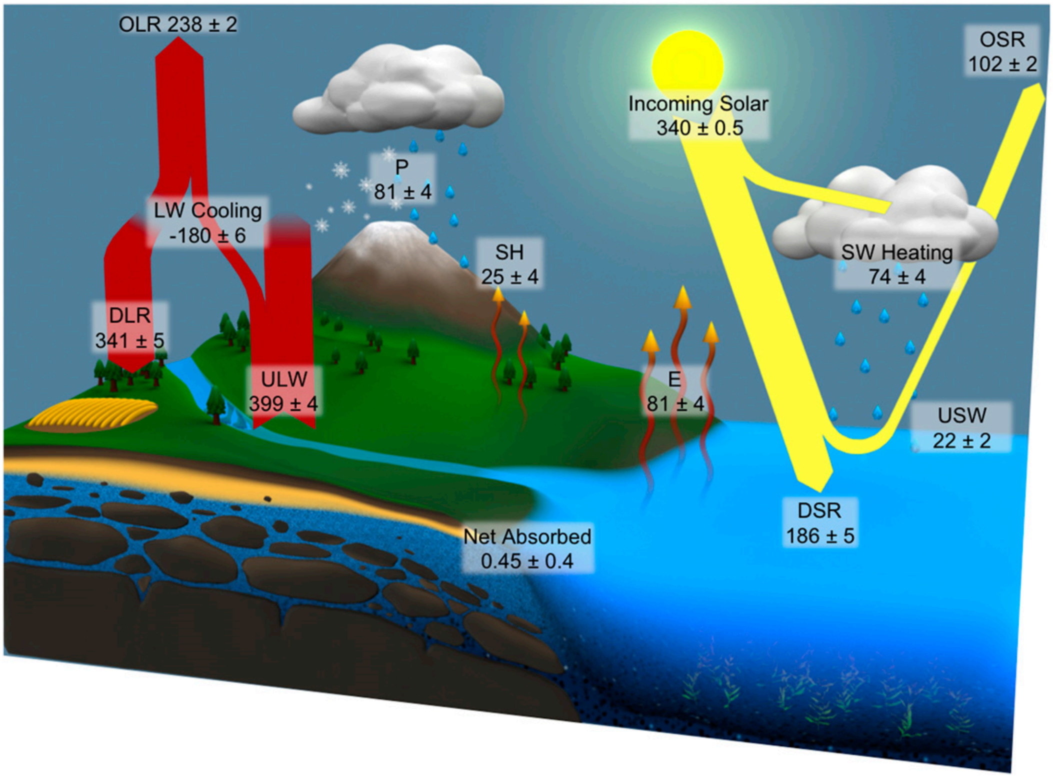

FIG. 4. As in Fig. 1, but after application of relevant energy and water cycle balance constraints.

the ocean surface has been diminished in all basins through reductions to both DLR and DSR, while precipitation and evaporation have both increased. Over continents the picture is more varied, with surface radiation increasing over Africa and to a lesser extent South America, Australia, and Eurasia but decreasing over North America and Antarctica. Latent and sensible heat adjustments mirror those in radiation, increasing over continents where radiation is reduced and decreasing over continents where radiation is increased. Once converted to flux units (by dividing by 0.147 and 0.364, respectively) the continent and ocean rows of Table 4 show remarkable agreement with the separate land and ocean energy budgets presented in Wild et al. (2015). The partitioning of ULW, DLR, and ET between land and oceans all agree within 3 W m^{-2}. As noted in Wild et al. (2015), despite significant differences in their distribution with latitude, DSR is almost identical over land and ocean regions, 185 and 187 W m^{-2}, respectively, compared to 185 and 184 W m^{-2} reported in Wild et al. (2015). The most significant exception concerns SH flux estimates that are more than 15% larger over both land and oceans in the present study, reflecting the potential for large biases in these estimates from both satellites and reanalyses and justifying the large uncertainties assigned to this quantity in the current study.

The effect of imposing balance constraints is clearly evident in the global distribution of annually averaged energy into the surface after optimization (see Fig. 5d). The component fluxes are now balanced over all continents as anticipated. While the energy budgets of individual basins do not necessarily balance since heat can be exchanged between basins, imbalances are significantly smaller than those in Fig. 2d and now exhibit the combination of surpluses and deficits necessary to support Eq. (13). The Gulf of Mexico and Caribbean Sea, for example, exhibit strong heating that likely balances weak overall cooling in the much larger North Atlantic basin.

The refinements to all annually averaged surface energy fluxes in each continent and ocean basin are isolated in Fig. 6. As in the global case, adjustments generally fall within the ranges implied by the uncertainties in each component flux, but several oceanic adjustments approach the maximum allowed by their uncertainties. This, coupled with the fact that fluxes tend to be adjusted in the same sense (increased or decreased) in all basins, suggests that biases exist in some of the component fluxes. Latent heat fluxes (both precipitation and evaporation) are generally adjusted by smaller increments in the current optimization than is argued by Stephens et al. (2012b), likely owing to the additional water cycle constraints applied in the current

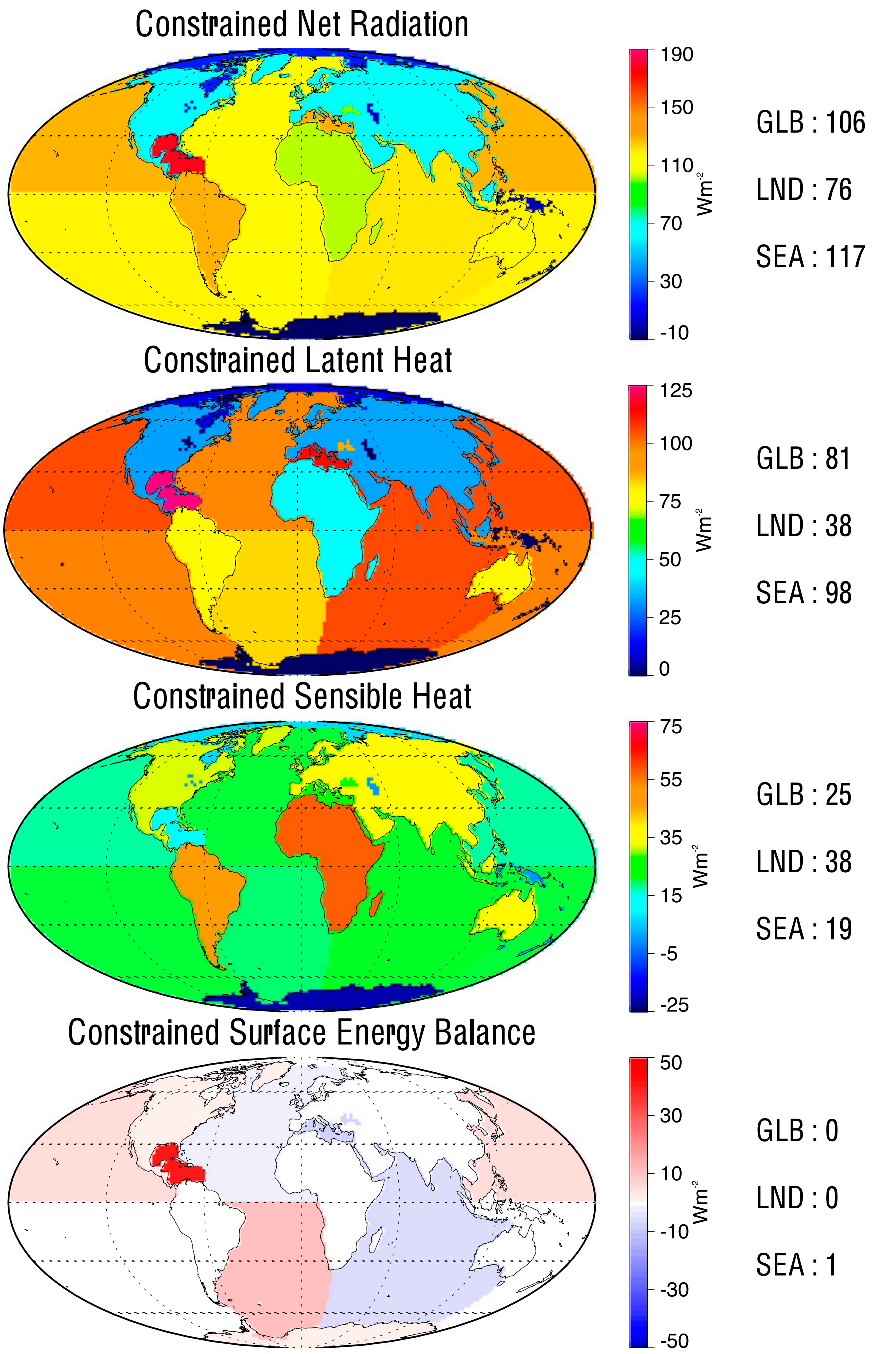

Constrained Net Radiation

Constrained Latent Heat

Constrained Sensible Heat

Constrained Surface Energy Balance

FIG. 5. Net energy exchange from the atmosphere to the surface after objectively introducing all relevant continental-scale energy and water cycle constraints.

analysis. The physical coupling of the energy and water cycles introduced in the joint analysis of this study and its companion, Rodell et al. (2015), allows other hydrologic parameters such as runoff and atmospheric moisture convergence to influence the magnitudes of the adjustments in the current analysis. Thus, while initial energy imbalances suggest that latent heating should be increased significantly, water cycle constraints limit the magnitude of the adjustments since precipitation already exceeds the sum of evaporation and runoff [see Rodell et al. (2015) for additional details]. Residual imbalances are therefore transferred to the radiative fluxes, resulting in larger adjustments to DLR and DSR. Although there is no way to demonstrate that the adjustments presented

TABLE 4. As in Table 2, but after imposing relevant energy and water balance constraints.

Map	Continent/basin	*P*	LE	DLR	DSR	ULW	USW	SH
01	North America	1.41 ± 0.06	0.79 ± 0.06	6.90 ± 0.12	3.65 ± 0.15	8.33 ± 0.12	0.66 ± 0.08	0.77 ± 0.15
02	South America	2.34 ± 0.09	1.37 ± 0.07	6.69 ± 0.09	3.75 ± 0.12	7.70 ± 0.07	0.46 ± 0.06	0.92 ± 0.11
03	Eurasia	3.05 ± 0.16	1.78 ± 0.18	15.9 ± 0.40	8.76 ± 0.44	19.3 ± 0.54	1.78 ± 0.12	1.82 ± 0.35
04	Africa	1.63 ± 0.07	1.33 ± 0.07	11.0 ± 0.19	7.41 ± 0.24	13.7 ± 0.17	1.67 ± 0.06	1.73 ± 0.19
05	Australia	0.31 ± 0.02	0.20 ± 0.02	2.72 ± 0.07	1.82 ± 0.08	3.43 ± 0.09	0.33 ± 0.05	0.58 ± 0.06
06	Island continent	0.30 ± 0.02	0.11 ± 0.02	0.53 ± 0.02	0.25 ± 0.02	0.60 ± 0.02	0.02 ± 0.01	0.05 ± 0.02
07	Antarctica	0.19 ± 0.03	0.01 ± 0.01	1.64 ± 0.16	1.58 ± 0.12	2.20 ± 0.08	1.27 ± 0.12	−0.2 ± 0.09
08	Arctic Ocean	0.270 ± 0.11	0.10 ± 0.02	2.31 ± 0.07	0.98 ± 0.04	2.61 ± 0.03	0.51 ± 0.09	0.07 ± 0.03
09	Caribbean Sea	0.370 ± 0.04	0.54 ± 0.05	1.75 ± 0.03	1.06 ± 0.03	1.99 ± 0.01	0.05 ± 0.01	0.05 ± 0.02
10	Mediterranean Sea	0.120 ± 0.02	0.29 ± 0.04	0.90 ± 0.02	0.56 ± 0.03	1.09 ± 0.01	0.03 ± 0.01	0.06 ± 0.02
11	Black Sea	0.030 ± 0.01	0.04 ± 0.01	0.15 ± 0.01	0.08 ± 0.01	0.18 ± 0.01	0.00 ± 0.01	0.01 ± 0.01
12	North Pacific	9.450 ± 0.74	8.62 ± 0.69	30.6 ± 0.51	16.1 ± 0.47	35.4 ± 0.31	0.99 ± 0.09	1.44 ± 0.29
13	North Atlantic	3.640 ± 0.38	4.27 ± 0.33	15.4 ± 0.23	7.92 ± 0.27	17.8 ± 0.17	0.51 ± 0.04	0.88 ± 0.18
14	Indian Ocean	6.720 ± 0.65	7.97 ± 0.69	26.7 ± 0.38	14.0 ± 0.40	30.8 ± 0.23	0.95 ± 0.07	1.56 ± 0.31
15	South Pacific	8.680 ± 0.81	9.90 ± 0.76	34.8 ± 0.55	18.9 ± 0.36	40.7 ± 0.33	1.37 ± 0.09	2.01 ± 0.37
16	South Atlantic	2.700 ± 0.37	3.86 ± 0.28	15.6 ± 0.18	8.14 ± 0.28	17.8 ± 0.14	0.71 ± 0.08	0.89 ± 0.18
—	Continents	9.23 ± 0.41	5.60 ± 0.40	45.5 ± 1.02	27.2 ± 1.13	55.3 ± 1.06	6.19 ± 0.48	5.60 ± 0.93
—	Oceans	31.9 ± 1.76	35.6 ± 1.76	128. ± 1.68	67.9 ± 1.63	148. ± 1.14	5.13 ± 0.43	6.98 ± 1.28
—	Global	41.2 ± 2.17	41.2 ± 2.16	174. ± 2.69	95.1 ± 2.75	203. ± 2.19	11.3 ± 0.90	12.5 ± 2.21

here are more realistic than those proposed elsewhere, they have the advantage that the methodology guarantees that the resulting fluxes satisfy both energy and water cycle constraints.

d. *Seasonal cycles*

In most locations the largest regional climate fluctuations are modulated by seasonal variations in solar insolation. Annual cycles of regional energy budgets therefore provide a first-order mode of climate variability that must be captured if we are to predict more subtle interannual changes. One of the advantages of the blending methodology introduced above is that it is fully scalable to problems with larger dimensionality, provided suitable energy and water cycle closure constraints can be defined. As a result, the methodology is an ideal tool for documenting the seasonal cycle of all component energy fluxes on continental and ocean-basin scales subject to monthly equivalents to the constraints listed above. Estimates of the uncertainty in each monthly mean flux are derived using the same procedure outlined in section 2 but are not reported explicitly in the interest of space.

The seasonal cycles of all fluxes contributing to TOA energy balance are summarized in Figs. 7 and 8 for all continents and ocean basins, respectively. For brevity, only optimally blended results are shown, and fluxes have been plotted in watts per square meter to facilitate displaying all regions in a single figure. Values should be multiplied by the appropriate areas in Table 2 to accurately reflect the partitioning of energy between regions. With the exception of Africa, net TOA radiation exhibits an annual period wave mode in all regions that tracks the periodicity of solar radiation. The magnitudes of the annual variations in net shortwave and outgoing longwave radiation over the continents agree well with those depicted in Trenberth and Fasullo (2013a), and, as in that study, peak emission of longwave radiation generally lags the peak in net solar radiation by one to two months (e.g., North America and Eurasia). Africa, on the other hand, exhibits a unique bimodal structure in net radiative balance at the TOA with peaks in the spring and fall seasons. This is consistent with the results of Trenberth and Fasullo (2013a) who point out that this is caused by Africa's comparable areas north and south of the equator and double monsoon.

Equivalent seasonal cycles in surface fluxes are presented in Fig. 9 (continents) and Fig. 10 (basins). Lags in longwave fluxes relative to shortwave fluxes are enhanced over the oceans and muted over the continents relative to the TOA. For example, peaks in both longwave emission and DLR lag surface shortwave radiation by at least two months over all major ocean basins, whereas the peaks in all radiative fluxes generally coincide over land. As one might expect this result is consistent with previous analyses of the seasonal cycle of surface temperature [see Trenberth (1983) and references therein] and reflects the lag in ocean temperature response to heating due to the large heat capacity of oceans relative to land. It also suggests that changes in atmospheric properties strongly modulate the connection between peak surface emission and OLR over continents.

In all ocean basins, turbulent heat transfer is dominated by latent heating from evapotranspiration. In the large ocean basins, summertime minima and wintertime

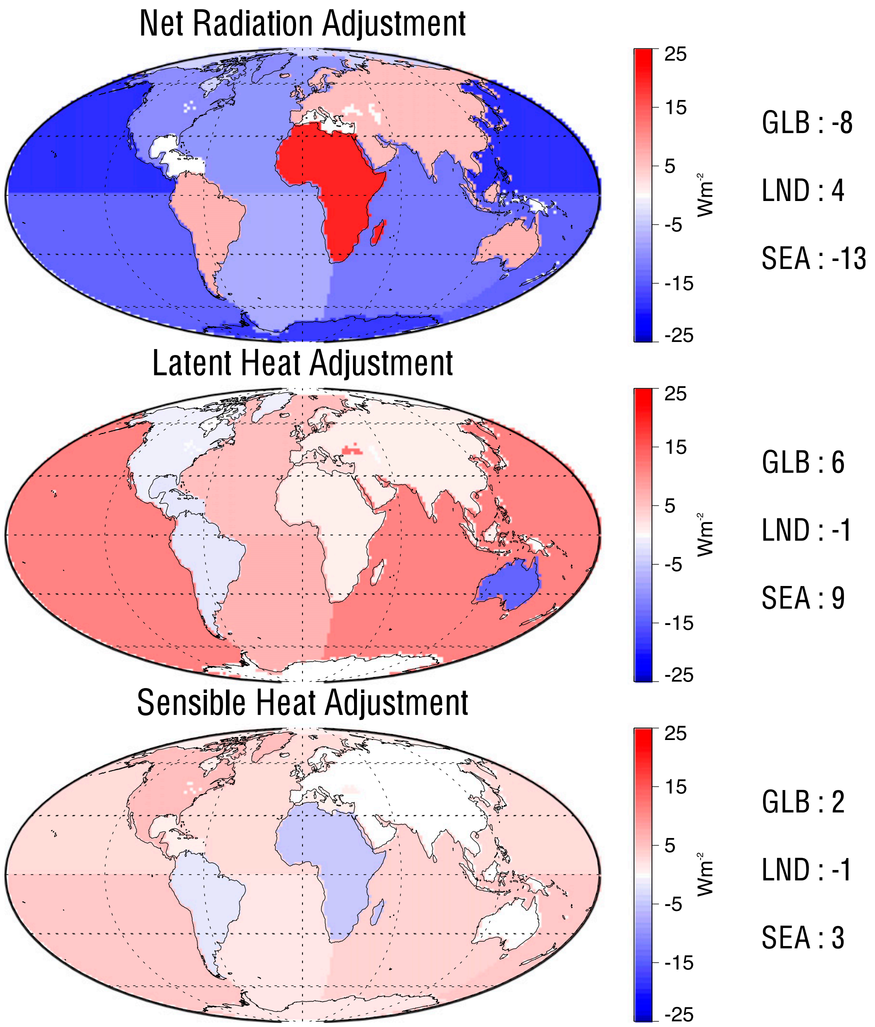

FIG. 6. Adjustments to radiation, sensible heat, and latent heat fluxes during the optimization process.

peaks in evaporation tend to reinforce the annual cycle in solar insolation into the oceans, causing large seasonal reversals in the net energy exchanged between the oceans and overlying atmosphere. Residuals in annual net heat exchange for individual basins are generally less than 10% of the amplitude of the seasonal cycle (Fig. 5). Over the continents, latent and sensible heat both contribute to the net turbulent heat transfer between the surface and the atmosphere, significantly enhancing the seasonal cycle in fluxes of energy from the surface to the atmosphere. The observed summer maxima and winter minima in turbulent heat fluxes over land play an important role in balancing corresponding changes in DSR, leading to seasonal cycles in net energy exchange between land surfaces and the overlying atmosphere with amplitudes generally less than 4% of the component upwelling and downwelling fluxes.

There are substantial hemispheric asymmetries in the polar regions, with Antarctica on average 20 K colder and 10% brighter than the Arctic. The coldest monthly surface emission observed on Earth is 147 W m^{-2} in Antarctica in August, corresponding to a mean surface temperature of 225 K. By comparison, the minimum monthly emitted flux in the Arctic is 203 W m^{-2} in February, implying a minimum temperature of 245 K. The Arctic also exhibits far stronger variations in TOA net radiation over the course of the year, losing more than 180 W m^{-2} in November while gaining a small 20 W m^{-2} in July, consistent with the CERES-based estimates reported in Porter et al. (2009). The magnitude of the observed annual cycle in TOA radiation generally agrees with Arctic energy balance reconstructions based on the 40-yr ECMWF Re-Analysis, the NCEP–NCAR 40-Year Reanalysis, and the Japanese 25-year Reanalysis Project

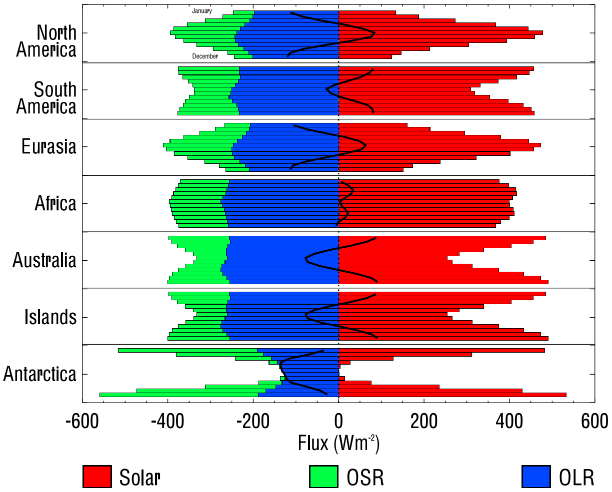

FIG. 7. Annual cycle of TOA radiative fluxes for each continent defined in Fig. 2. The heavy black line represents the net radiation into the region.

to within the stated uncertainties, although the reanalyses consistently place the maximum in June as opposed to July (Serreze et al. 2007; Porter et al. 2009). By contrast, the present work indicates that Antarctica does not experience a surplus of TOA radiation at any time of year but also never loses more than 150 W m^{-2} to space. At the surface, both regions experience net energy gains in the summer months that are offset by corresponding energy losses in the winter, but there is a clear seasonal asymmetry in the net energy exchange between the atmosphere and surface in the Arctic owing to the buffering effects of sea ice that shift the peak surface reflection and emission relative to incoming solar radiation.

Another general observation can be made regarding balance on regional scales: as time and space scales are reduced, satisfying relevant budget constraints becomes increasingly difficult because of the increased likelihood of structural biases in the relevant observational datasets. For example, the annual continental-scale optimization involves 73 degrees of freedom and results in $\chi^2 = 21$, while the monthly continental-scale optimization results in $\chi^2 = 547$ with 660 degrees of freedom. Thus, while χ^2 indicates an acceptable overall fit in both cases, the average adjustment approaches the magnitude of the assumed uncertainties in the annual-cycle continental-scale optimization. Closer comparison of the final flux estimates on the scales of individual continents and basins reveals that energy budget residuals (given by the sum of the adjustments to individual flux components) are found to fall within error bounds over all continents and in the smaller Caribbean, Mediterranean, and Black Seas. Residuals in the North Pacific, South Pacific, and Indian Oceans, however, all exceed associated closure errors. In these regions, adjustments to DLR, DSR, and latent heat fluxes all exceed their corresponding uncertainty estimates, confirming the presence of biases in some of the component energy fluxes on these scales that can likely be attributed to the sources of structural error listed above.

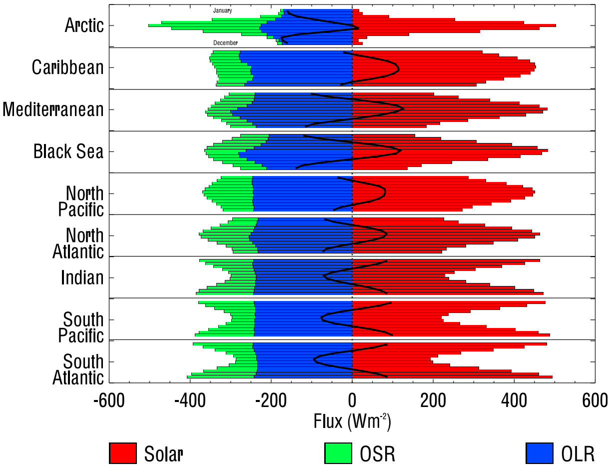

FIG. 8. As in Fig. 7, but for each ocean basin.

5. Discussion

Recent attempts to document the global energy balance using modern satellite datasets have yielded depictions of the global energy budget that differ in several key ways, most notably in their estimates of downwelling longwave radiation and atmospheric latent heat release. This paper revisits the issue of imbalances in observationally derived energy flux datasets with the goal of establishing objectively balanced reconstructions of the current state of the global energy budget and its distribution on continental and ocean-basin scales. Two sets of energy budget estimates are reported that address two important questions: "How well do current observations constrain the energy budget?" and "To what extent can balance be objectively imposed within rigorous estimates of the uncertainties in the component fluxes?"

In the absence of balance constraints, various combinations of modern satellite datasets suggest that globally and annually averaged surface radiative fluxes exceed corresponding turbulent energy fluxes by 13–24 W m^{-2}. These imbalances occur primarily in oceanic regions where all component fluxes are derived independently. The systematic manner by which downwelling radiative fluxes exceed turbulent heat fluxes across all major ocean basins is more indicative of biases than of random errors. This can be attributed to the complexities of deriving energy and water fluxes from remote measurements that

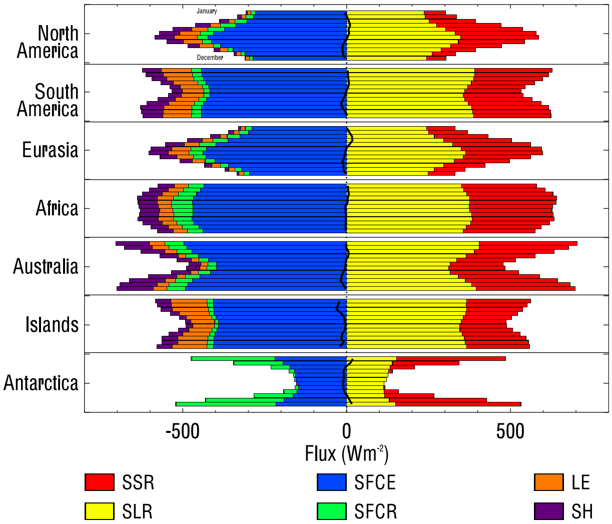

FIG. 9. Annual cycle of surface energy fluxes for each continent defined in Fig. 2. Net energy into the surface is presented as the heavy black line.

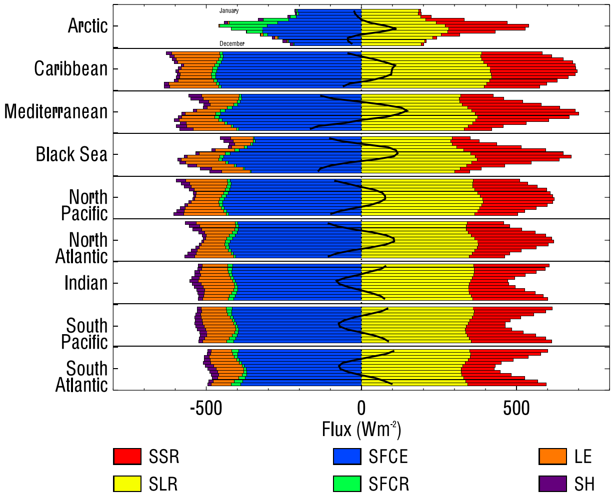

FIG. 10. As in Fig. 9, but for each ocean basin.

necessitate independent algorithms that use distinct observations and assumptions. Since each flux dataset is developed in isolation, valuable energy budget and water cycle closure information that could help mitigate biases is omitted.

In an effort to reintroduce this closure information and address the need for a balanced monthly, continental-scale energy budget dataset for documenting today's climate and evaluating its representation in models, a method has been developed to objectively impose well-defined global and regional energy and water balance constraints on the system. While the resulting flux estimates can no longer be traced to unique observational origins, they constitute a balanced ensemble that maintains consistency with the original component datasets and their estimated uncertainties. After optimization, energy balance residuals are generally found to be less than closure errors, indicating that continental energy budgets can be balanced within the uncertainties in the component flux datasets. More generally, the results demonstrate that much of the discrepancy between other recent depictions of the global energy budget can, in fact, be explained within the error bounds of the component fluxes. On the other hand, the magnitude of the adjustments required to achieve balance in some regions lies near the extremes implied by the prescribed uncertainty ranges, especially on monthly time scales, underscoring the need for reducing uncertainties in observation-based energy flux datasets in the future.

The fluxes generated in this study and its companion (Rodell et al. 2015) provide state-of-the-art reconstructions of energy flows and water fluxes at the beginning of the twenty-first century on monthly and continental scales that integrate the most current observational capabilities. The fluxes simultaneously satisfy all relevant energy and hydrologic cycle closure constraints while preserving the information contained in the original observationally derived datasets through direct use of rigorous uncertainty estimates. The resulting global energy balance reconstruction represents a compromise between other recent estimates. Precipitation and evaporation are in better agreement with the values reported by Trenberth et al. (2009), while estimates of DSR and sensible heating align better with the estimates of Stephens et al. (2012b). Overall, the current reconstruction most closely agrees with that of Wild et al. (2013), which derives primarily from surface-based observations. In particular, our estimates of DLR (or "back radiation" as it is sometimes termed) agree very well with those of Wild et al. (2013) as well as those reported in Wang and Dickinson (2013) but fall in between the estimates reported in Trenberth et al. (2009) and Stephens et al. (2012b). It is worth noting that our surface sensible heating estimate ($25\,\mathrm{W\,m^{-2}}$) exceeds the value listed in many current and historical reconstructions by 20%–30% and may warrant further investigation. The complete observational energy and water budget analysis described here and in the companion paper by Rodell et al. (2015) is available for download (GES DISC 2015). This dataset includes all energy and water cycle fluxes on continental and monthly space and time scales both prior to and after the addition of relevant balance constraints.

Despite its strengths, there are some important caveats associated with the current analysis. First, a decision was made to focus on the golden age of satellite observations in the first decade of the new millennium as opposed to developing a true climatology that is commonly defined to correspond to a 30-yr period. Given the recent advances in instrumentation over this period and the challenges associated with creating longer-term climate records from multiple satellite platforms, this choice may be justified, but it should be noted that the results presented here are influenced by decadal variability such as the Pacific decadal oscillation, which has been shown to have contributed to the reduced trends in global temperatures over the period examined here (Trenberth and Fasullo 2013a). On the other hand, trends that may be present in any of the component fluxes over the 10-yr period, such as melting of the Greenland ice sheet, were intentionally removed to avoid the influence of interannual variability. Also, while considerable effort was made to include information from a range of high-quality observational data sources, some datasets were chosen for inclusion in this study based on the expertise of the members of the NEWS team. In some cases, the methods used for combining datasets, establishing uncertainties, and using reanalyses to fill observational gaps were driven by convenience and may not be optimal under all conditions. Likewise, there is no rigorous justification for assuming that uncertainties in component fluxes are unbiased and Gaussian in the optimization. Biases in any of the component fluxes reduce the veracity of the resulting balanced flux estimates and associated uncertainty ranges. In the absence of quantitative information regarding such biases, however, it is not clear that alternative assumptions are justified or would yield dramatically different results given the magnitudes of the error bars.

The flexibility of the framework outlined here also offers several avenues for refinement. In the future, the focus on decade mean conditions should be relaxed to include interannual variability, and the spatial resolution of the analysis should be increased to better resolve the different climate zones on Earth. Such an expansion would benefit from the addition of several available constraints that were not included in the current analysis. Observational estimates of ocean heat transport and surface radiative fluxes and fluxes of dry and moist static energy derived from reanalyses could significantly expand the breadth of budget relationships employed in the optimization and help to establish consistency with these other valuable data sources. Including such observations may offer a pathway to bridge the remaining discrepancies between modern energy budget reconstructions and generating energy and water cycle estimates on the scales desired for regional climate applications. As noted above, the systematic nature of the flux adjustments required to achieve balance suggests that biases are present in several of the component flux datasets. While the magnitudes of these biases are not inconsistent with the uncertainty estimates provided here, additional refinement of the algorithms used to derive component fluxes is clearly warranted. For example, improving the microphysical property assumptions employed in global precipitation algorithms, refining the near-surface temperature and humidity estimates and bulk formulas governing estimates of surface turbulent heat fluxes, and fine-tuning methods employed to represent the diurnal cycle of solar radiation, clouds, and surface temperature in surface radiative fluxes all offer the potential to improve regional energy budget estimates.

It should be emphasized that the new energy balance reconstructions presented here relied heavily on the recent advances in Earth-observing capabilities provided by the TRMM, GRACE, *Aqua*, *Terra*, *Aura*, *CloudSat*, and *CALIPSO* satellites and corresponding tools for integrating these measurements into assimilation systems like MERRA and GLDAS. The results point to a need for continued observation and refinement of satellite flux algorithms, yet all of these missions are now operating well beyond their design lifetimes, in some cases without concrete plans for a successor. Given the importance of observing climate variability, systematic planning for future missions with new technologies for improving the absolute accuracy of component fluxes and establishing the factors that modify them is critical. Particular attention should be given to quantifying biases in component fluxes on regional scales, and it is anticipated that analysis of data from the recently launched Global Precipitation Measurement (GPM), Soil Moisture Active Passive (SMAP), and *Suomi–National Polar-Orbiting Partnership* (*Suomi NPP*) missions will facilitate progress toward this goal. The approach outlined here provides a framework for integrating these new observations and reintroducing relevant balance information to identify biases. As uncertainties in observational datasets are reduced through new technology and refined algorithms, it may no longer be possible to objectively achieve balance. Such a breakdown (indicated by either large χ^2 or unrealistically large adjustments to one or more fluxes) would provide direct evidence of biases in individual datasets.

Acknowledgments. This study is the result of a collaboration of multiple investigators each supported by the NEWS program. The goal of NEWS is to foster large collaborative research activities that cross traditional disciplinary boundaries to improve understanding and prediction of the global energy and water cycles. All data generated in the course of this work can be accessed through GES DISC (2015). This dataset summarizes the original observationally based estimates of all component fluxes for each continent and ocean basin on monthly and annual scales as well as means over all oceans, means over all continents, and the global mean. A companion dataset provides optimized versions of all component fluxes in the same format. GEWEX SRB data were obtained from the NASA Langley Research Center Atmospheric Science Data Center NASA/GEWEX SRB Project (GEWEX 2007). The C3M product (edition B1) was obtained from the Atmospheric Science Data Center (ASDC 2012). ISCCP D2 data were obtained from the International Satellite Cloud Climatology Project maintained by the ISCCP research group at the NASA Goddard Institute for Space Studies in New York, New York (ISCCP 2007). 2B-FLXHR-lidar data were obtained through the *CloudSat* Data Processing Center (DPC 2011). The GPCP combined precipitation data were provided by the NASA Goddard Space Flight Center's Laboratory for Atmospheres (GPCP 2009), which develops and computes the dataset as a contribution to the GEWEX Global Precipitation Climatology Project. MERRA data used in this study have been provided by the Global Modeling and Assimilation Office (GMAO) at NASA Goddard Space Flight Center (GMAO 2013). Part of the research was carried out at the Jet Propulsion Laboratory, California Institute of Technology, under a contract with the National Aeronautics and Space Administration.

REFERENCES

Abbot, C. G., and F. E. Fowle, 1908: Radiation and terrestrial temperature. *Ann. Astrophys. Obs. Smithson. Inst.*, **2**, 125–224.

Adler, R. F., and Coauthors, 2003: The Version-2 Global Precipitation Climatology Project (GPCP) monthly precipitation analysis (1979–present). *J. Hydrometeor.*, **4**, 1147–1167, doi:10.1175/1525-7541(2003)004<1147:TVGPCP>2.0.CO;2.

——, G. Gu, and G. J. Huffman, 2012: Estimating climatological bias errors for the Global Precipitation Climatology Project (GPCP). *J. Appl. Meteor. Climatol.*, **51**, 84–99, doi:10.1175/JAMC-D-11-052.1.

ASDC, 2012: CERES-CALIPSO-CloudSat-MODIS (C3M), version B1. Langley Atmospheric Science Data Center, accessed June 2013. [Available online at https://eosweb.larc.nasa.gov/project/ceres/cccm_table.]

Barker, H. W., J.-J. Morcrette, and G. D. Alexander, 1998: Broadband solar fluxes and heating rates for atmospheres with 3D broken clouds. *Quart. J. Roy. Meteor. Soc.*, **124**, 1245–1271, doi:10.1002/qj.49712454811.

Behrangi, A., G. Stephens, R. F. Adler, G. J. Huffman, B. Lambrigtsen, and M. Lebsock, 2014: An update on the oceanic precipitation rate and its zonal distribution in light of advanced observations from space. *J. Climate*, **27**, 3957–3965, doi:10.1175/JCLI-D-13-00679.1.

Benner, T. C., J. A. Curry, and J. O. Pinto, 2001: Radiative transfer in the summertime Arctic. *J. Geophys. Res.*, **106**, 15 173–15 183, doi:10.1029/2000JD900422.

Berg, W., C. Kummerow, and C. A. Morales, 2002: Differences between east and west Pacific rainfall systems. *J. Climate*, **15**, 3659–3672, doi:10.1175/1520-0442(2002)015<3659:DBEAWP>2.0.CO;2.

——, T. L'Ecuyer, and C. Kummerow, 2006: Rainfall climate regimes: The relationship of regional TRMM rainfall biases to the environment. *J. Appl. Meteor. Climatol.*, **45**, 434–454, doi:10.1175/JAM2331.1.

——, ——, and J. M. Haynes, 2010: The distribution of rainfall over oceans from spaceborne radars. *J. Appl. Meteor. Climatol.*, **49**, 535–543, doi:10.1175/2009JAMC2330.1.

Bonan, G. B., 1998: The land surface climatology of the NCAR Land Surface Model coupled to the NCAR Community Climate Model. *J. Climate*, **11**, 1307–1326, doi:10.1175/1520-0442(1998)011<1307:TLSCOT>2.0.CO;2.

Bony, S., and Coauthors, 2006: How well do we understand and evaluate climate change feedback processes? *J. Climate*, **19**, 3445–3482, doi:10.1175/JCLI3819.1.

Bosilovich, M. G., and S. D. Schubert, 2001: Precipitation recycling over the central United States as diagnosed from the GEOS-1 Data Assimilation System. *J. Hydrometeor.*, **2**, 26–35, doi:10.1175/1525-7541(2001)002<0026:PROTCU>2.0.CO;2.

——, and Coauthors, 2006: NASA's Modern Era Retrospective-Analysis for Research and Applications. *U.S. CLIVAR Variations*, No. 4, 5–8.

——, F. R. Robertson, and J. Chen, 2011: Global energy and water budgets in MERRA. *J. Climate*, **24**, 5721–5739, doi:10.1175/2011JCLI4175.1.

Brown, P. J., and C. D. Kummerow, 2014: An assessment of atmospheric water budget components over tropical oceans. *J. Climate*, **27**, 2054–2071, doi:10.1175/JCLI-D-13-00385.1.

Brunke, M. A., Z. Wang, X. Zeng, M. Bosilovich, and C.-L. Shie, 2011: An assessment of the uncertainties in ocean surface turbulent fluxes in 11 reanalysis, satellite-derived, and combined global datasets. *J. Climate*, **24**, 5469–5493, doi:10.1175/2011JCLI4223.1.

Budyko, M. I., 1974: *Climate and Life*. International Geophysics Series, Vol. 18, Academic Press, 508 pp.

Cairns, B., A. A. Lacis, and B. E. Carlson, 2000: Absorption within inhomogeneous clouds and its parameterization in general circulation models. *J. Atmos. Sci.*, **57**, 700–714, doi:10.1175/1520-0469(2000)057<0700:AWICAI>2.0.CO;2.

Chen, F., and Coauthors, 1996: Modeling of land surface evaporation by four schemes and comparison with FIFE observations. *J. Geophys. Res.*, **101**, 7251–7268, doi:10.1029/95JD02165.

Chung, E.-S., B. Soden, B. J. Sohn, and L. Shi, 2014: Upper-tropospheric moistening in response to anthropogenic warming. *Proc. Natl. Acad. Sci. USA*, **111**, 11 636–11 641, doi:10.1073/pnas.1409659111.

Clark, E. A., J. Sheffield, M. van Vliet, B. Nijssen, and D. P. Lettenmaier, 2015: Continental runoff into the oceans (1950–2008). *J. Hydrometeor.*, **16**, 1502–1520, doi:10.1175/JHM-D-14-0183.1.

Clayson, C. A., and A. Bogdanoff, 2013: The effect of diurnal sea surface temperature warming on climatological air–sea fluxes. *J. Climate*, **26**, 2546–2556, doi:10.1175/JCLI-D-12-00062.1.

Curry, J. A., and Coauthors, 2004: SeaFlux. *Bull. Amer. Meteor. Soc.*, **85**, 409–424, doi:10.1175/BAMS-85-3-409.

Dai, A., and K. E. Trenberth, 2004: The diurnal cycle and its depiction in the Community Climate System Model. *J. Climate*, **17**, 930–951, doi:10.1175/1520-0442(2004)017<0930:TDCAID>2.0.CO;2.

Dai, F., R. Yu, X. Zhang, Y. Yu, and J. Li, 2003: The impact of low-level cloud over the eastern subtropical Pacific on the "double ITCZ" in LASG FGCM-0. *Adv. Atmos. Sci.*, **20**, 461–474, doi:10.1007/BF02690804.

Davis, C. A., K. W. Manning, R. E. Carbone, S. B. Trier, and J. D. Tuttle, 2003: Coherence of warm-season continental rainfall in numerical weather prediction models. *Mon. Wea. Rev.*, **131**, 2667–2679, doi:10.1175/1520-0493(2003)131<2667:COWCRI>2.0.CO;2.

Dee, D., and Coauthors, 2011: The ERA-Interim reanalysis: Configuration and performance of the data assimilation system. *Quart. J. Roy. Meteor. Soc.*, **137**, 553–597, doi:10.1002/qj.828.

Dines, W. H., 1917: The heat balance of the atmosphere. *Quart. J. Roy. Meteor. Soc.*, **43**, 151–158, doi:10.1002/qj.49704318203.

DPC, 2011: CloudSat Level 2B Fluxes and Heating Rates (2B-FLXHR-LIDAR), release 04. CloudSat Data Processing Center, accessed January 2011. [Available online at http://www.cloudsat.cira.colostate.edu.]

Ek, M. B., K. E. Mitchell, Y. Lin, E. Rogers, P. Grunmann, V. Koren, G. Gayno, and J. D. Tarpley, 2003: Implementation of Noah land surface model advances in the National Centers for Environmental Prediction operational mesoscale Eta Model. *J. Geophys. Res.*, **108**, 8851, doi:10.1029/2002JD003296.

Fasullo, J. T., and K. E. Trenberth, 2008a: The annual cycle of the energy budget. Part I: Global mean and land–ocean exchanges. *J. Climate*, **21**, 2297–2312, doi:10.1175/2007JCLI1935.1.

——, and ——, 2008b: The annual cycle of the energy budget. Part II: Meridional structures and poleward transports. *J. Climate*, **21**, 2313–2325, doi:10.1175/2007JCLI1936.1.

GES DISC, 2015: NASA Energy and Water Cycle Study (NEWS) energy and water cycle climatology dataset, version 1. Goddard Earth Science Data and Information Service Center, accessed August 2015. [Available online at http://disc.gsfc.nasa.gov/hydrology.]

GEWEX, 2007: Global Energy and Water Cycle Experiment (GEWEX) Surface Radiation Budget (SRB), release 3.0. Langley Atmospheric Science Data Center, accessed January 2011. [Available online at https://eosweb.larc.nasa.gov/project/srb/srb_table/.]

GMAO, 2013: Modern Era Retrospecive Analysis for Research and Applications, version 2.3. Global Modeling and Assimilation Office, Goddard Space Flight Center, accessed January 2011. [Available online at http://gmao.gsfc.nasa.gov/merra/.]

GPCP, 2009: Global Precipitation Climatology Project 1-degree Daily Global Precipitation Analysis, version 2.2. Goddard Space Flight Center, accessed January 2011. [Available online at http://precip.gsfc.nasa.gov.]

Grabowski, W. W., and Coauthors, 2006: Daytime convective development over land: A model intercomparison based on LBA observations. *Quart. J. Roy. Meteor. Soc.*, **132**, 317–344, doi:10.1256/qj.04.147.

Gulev, S., T. Jung, and E. Ruprecht, 2007a: Estimation of the impact of sampling errors in the VOS observations on air–sea fluxes. Part I: Uncertainties in climate means. *J. Climate*, **20**, 279–301, doi:10.1175/JCLI4010.1.

——, ——, and ——, 2007b: Estimation of the impact of sampling errors in the VOS observations on air–sea fluxes. Part II: Impact on trends and interannual variability. *J. Climate*, **20**, 302–315, doi:10.1175/JCLI4008.1.

Gupta, S. K., N. A. Ritchey, A. C. Wilber, C. H. Whitlock, G. G. Gibson, and P. W. Stackhouse, 1999: A climatology of surface radiation budget derived from satellite data. *J. Climate*, **12**, 2691–2710, doi:10.1175/1520-0442(1999)012<2691:ACOSRB>2.0.CO;2.

Ham, S.-H., S. Kato, H. W. Barker, F. G. Rose, and S. Sun-Mack, 2014: Effects of 3-D clouds on atmospheric transmission of solar radiation: Cloud type dependencies inferred from A-train satellite data. *J. Geophys. Res. Atmos.*, **119**, 943–963, doi:10.1002/2013JD020683.

Hansen, M. C., R. S. DeFries, J. R. G. Townshend, and R. Sohlberg, 2000: Global land cover classification at 1 km spatial resolution using a classification tree approach. *Int. J. Remote Sens.*, **21**, 1331–1364, doi:10.1080/014311600210209.

Hartmann, D. L., 1994: *Global Physical Climatology*. International Geophysics Series, Vol. 56, Academic Press, 411 pp.

——, H. H. Hendon, and R. A. Houze Jr., 1984: Some implications of the mesoscale circulations in tropical cloud clusters for large-scale dynamics and climate. *J. Atmos. Sci.*, **41**, 113–121, doi:10.1175/1520-0469(1984)041<0113:SIOTMC>2.0.CO;2.

Henderson, D. S., T. L'Ecuyer, G. Stephens, P. Partain, and M. Sekiguchi, 2013: A multisensor perspective on the radiative impacts of clouds and aerosols. *J. Appl. Meteor. Climatol.*, **52**, 853–871, doi:10.1175/JAMC-D-12-025.1.

Hilburn, K. A., 2009: The passive microwave water cycle product. Remote Sensing Systems Tech. Rep. 072409, 30 pp. [Available online at ftp://ftp.remss.com/water_cycle/Hilburn_water_cycle_REMSS_TR_072409.pdf.]

Huffman, G. J., R. F. Adler, M. Morrissey, D. Bolvin, S. Curtis, R. Joyce, B. McGavock, and J. Susskind, 2001: Global precipitation at one-degree daily resolution from multisatellite observations. *J. Hydrometeor.*, **2**, 36–50, doi:10.1175/1525-7541(2001)002<0036:GPAODD>2.0.CO;2.

——, ——, D. Bolvin, and G. Gu, 2009: Improving the global precipitation record: GPCP version 2.1. *Geophys. Res. Lett.*, **36**, doi:10.1029/2009GL040000.

Idso, S., 1981: A set of equations for full spectrum and 8- to 14-μm and 10.5- to 12.5-μm thermal radiation from cloudless skies. *Water Resour. Res.*, **17**, 295–304, doi:10.1029/WR017i002p00295.

ISCCP, 2007: International Satellite Cloud Climatology Project (ISCCP) Global and Surface Radiative Fluxes (FD). Goddard Institute for Space Studies, accessed January 2011. [Available online at http://isccp.giss.nasa.gov.]

Jiménez, C., and Coauthors, 2011: Global intercomparison of 12 land surface heat flux estimates. *J. Geophys. Res.*, **116**, D02102, doi:10.1029/2010JD014545.

Josey, S. A., L. Yu, S. Gulev, X. Jin, N. Tilinina, B. Barnier, and L. Brodeau, 2014: Unexpected impacts of the tropical Pacific array on reanalysis surface meteorology and heat fluxes. *Geophys. Res. Lett.*, **41**, 6213–6220, doi:10.1002/2014GL061302.

Kalnay, E., 2003: *Atmospheric Modeling, Data Assimilation and Predictability*. Cambridge University Press, 364 pp.

——, and Coauthors, 1996: The NCEP/NCAR 40-Year Reanalysis Project. *Bull. Amer. Meteor. Soc.*, **77**, 437–471, doi:10.1175/1520-0477(1996)077<0437:TNYRP>2.0.CO;2.

Kato, S., S. Sun-Mack, W. F. Miller, F. G. Rose, Y. Chen, P. Minnis, and B. A. Wielicki, 2010: Relationships among cloud occurrence frequency, overlap, and effective thickness derived from *CALIPSO* and *CloudSat* merged cloud vertical profiles. *J. Geophys. Res.*, **115**, D00H28, doi:10.1029/2009JD012277.

——, and Coauthors, 2011: Improvements of top-of-atmosphere and surface irradiance computations with *CALIPSO*-, *CloudSat*-, and MODIS-derived cloud and aerosol properties. *J. Geophys. Res.*, **116**, D19209, doi:10.1029/2011JD016050.

——, N. G. Loeb, D. A. Rutan, F. G. Rose, S. Sun-Mack, W. F. Miller, and Y. Chen, 2012: Uncertainty estimate of surface irradiances computed with MODIS-, *CALIPSO*-, and *CloudSat*-derived cloud and aerosol properties. *Surv. Geophys.*, **33**, 395–412, doi:10.1007/s10712-012-9179-x.

——, ——, F. G. Rose, D. R. Doelling, D. A. Rutan, T. E. Caldwell, L. Yu, and R. A. Weller, 2013: Surface irradiances consistent with CERES-derived top-of-atmosphere shortwave and longwave irradiances. *J. Climate*, **26**, 2719–2740, doi:10.1175/JCLI-D-12-00436.1.

Kay, J. E., and Coauthors, 2012: Exposing global cloud biases in the Community Atmosphere Model (CAM) using satellite observations and their corresponding instrument simulators. *J. Climate*, **25**, 5190–5207, doi:10.1175/JCLI-D-11-00469.1.

Kiehl, J. T., and K. E. Trenberth, 1997: Earth's annual global mean energy budget. *Bull. Amer. Meteor. Soc.*, **78**, 197–208, doi:10.1175/1520-0477(1997)078<0197:EAGMEB>2.0.CO;2.

Kopp, G., and J. L. Lean, 2011: A new, lower value of total solar irradiance: Evidence and climate significance. *Geophys. Res. Lett.*, **38**, L01706, doi:10.1029/2010GL045777.

Koren, V., J. Schaake, K. Mitchell, Q.-Y. Duan, F. Chen, and J. M. Baker, 1999: A parameterization of snowpack and frozen ground intended for NCEP weather and climate models. *J. Geophys. Res.*, **104**, 19 569–19 585, doi:10.1029/1999JD900232.

Koster, R. D., and M. J. Suarez, 1996: Energy and water balance calculations in the Mosaic LSM. NASA Tech. Memo. 104606, 60 pp. [Available online at http://gmao.gsfc.nasa.gov/pubs/docs/Koster130.pdf.]

Kumar, S. V., and Coauthors, 2006: Land information system: An interoperable framework for high resolution land surface modeling. *Environ. Modell. Software*, **21**, 1402–1415, doi:10.1016/j.envsoft.2005.07.004.

Landerer, F. W., and S. C. Swenson, 2012: Accuracy of scaled GRACE terrestrial water storage estimates. *Water Resour. Res.*, **48**, W04531, doi:10.1029/2011WR011453.

Lau, K.-M., and L. Peng, 1987: Origin of low-frequency (intraseasonal) oscillations in the tropical atmosphere. Part I: Basic theory. *J. Atmos. Sci.*, **44**, 950–972, doi:10.1175/1520-0469(1987)044<0950:OOLFOI>2.0.CO;2.

L'Ecuyer, T. S., and G. L. Stephens, 2002: An estimation-based precipitation retrieval algorithm for attenuating radars. *J. Appl. Meteor.*, **41**, 272–285, doi:10.1175/1520-0450(2002)041<0272:AEBPRA>2.0.CO;2.

——, and ——, 2003: The tropical oceanic energy budget from the TRMM perspective. Part I: Algorithm and uncertainties. *J. Climate*, **16**, 1967–1984, doi:10.1175/1520-0442(2003)016<1967:TTOEBF>2.0.CO;2.

——, and ——, 2007: The tropical atmospheric energy budget from the TRMM perspective. Part II: Evaluating GCM representations of the sensitivity of regional energy and water cycles to the 1998–99 ENSO cycle. *J. Climate*, **20**, 4548–4571, doi:10.1175/JCLI4207.1.

——, N. B. Wood, T. Haladay, G. L. Stephens, and P. W. Stackhouse Jr., 2008: Impact of clouds on atmospheric heating based on the R04 *CloudSat* fluxes and heating rates data set. *J. Geophys. Res.*, **113**, D00A15, doi:10.1029/2008JD009951.

Lee, M.-I., I.-S. Kang, J.-K. Kim, and B. E. Mapes, 2001: Influence of cloud-radiation interaction on simulating tropical intraseasonal oscillation with an atmospheric general circulation model. *J. Geophys. Res.*, **106**, 14 219–14 233, doi:10.1029/2001JD900143.

Li, J. L., X. H. Zhang, Y. Q. Yu, and F. S. Dai, 2004: Primary reasoning behind the double ITCZ phenomenon in a coupled ocean-atmosphere general circulation model. *Adv. Atmos. Sci.*, **21**, 857–867, doi:10.1007/BF02915588.

Liang, X., D. P. Lettenmaier, E. F. Wood, and S. J. Burges, 1994: A simple hydrologically based model of land surface water and energy fluxes for general circulation models. *J. Geophys. Res.*, **99**, 14 415–14 428, doi:10.1029/94JD00483.

Lin, B., P. Stackhouse, P. Minnis, B. Wielicki, Y. Hu, W. Sun, T.-F. Fan, and L. Hinkelman, 2008: Assessment of global annual atmospheric energy balance from satellite observations. *J. Geophys. Res.*, **113**, D16114, doi:10.1029/2008JD009869.

Liou, K.-N., 1980: *An Introduction to Atmospheric Radiation*. International Geophysics Series, Vol. 84, Academic Press, 392 pp.

Liu, W. T., X. Xie, W. Tang, and V. Zlotnicki, 2006: Spacebased observations of oceanic influence on the annual variation of South American water balance. *Geophys. Res. Lett.*, **33**, L08710, doi:10.1029/2006GL025683.

Loeb, N. G., K. J. Priestley, D. P. Kratz, E. B. Geier, R. N. Green, B. Wielicki, P. O'Rawe Hinton, and S. K. Nolan, 2001: Determination of unfiltered radiances from the Clouds and the Earth's Radiation Energy System instrument. *J. Appl. Meteor.*, **40**, 822–835, doi:10.1175/1520-0450(2001)040<0822:DOURFT>2.0.CO;2.

——, B. A. Wielicki, D. R. Doelling, G. L. Smith, D. F. Keyes, S. Kato, N. Manalo-Smith, and T. Wong, 2009: Toward optimal closure of the earth's top-of-atmosphere radiation budget. *J. Climate*, **22**, 748–766, doi:10.1175/2008JCLI2637.1.

——, D. A. Rutan, S. Kato, and W. Wang, 2014: Observing interannual variations in Hadley circulation atmospheric diabatic heating and circulation strength. *J. Climate*, **27**, 4139–4158, doi:10.1175/JCLI-D-13-00656.1.

Luthcke, S. B., T. J. Sabaka, B. D. Loomis, A. A. Arendt, J. J. McCarthy, and J. Camp, 2013: Antarctica, Greenland and Gulf of Alaska land-ice evolution from an iterated GRACE global mascon solution. *J. Glaciol.*, **59**, 613–631, doi:10.3189/2013JoG12J147.

Lyman, J. M., S. A. Good, V. V. Gouretski, M. Ishii, G. C. Johnson, M. D. Palmer, D. M. Smith, and J. K. Willis, 2010: Robust warming of the global upper ocean. *Nature*, **465**, 334–337, doi:10.1038/nature09043.

Masunaga, H., and T. S. L'Ecuyer, 2010: The southeast Pacific warm band and double ITCZ. *J. Climate*, **23**, 1189–1208, doi:10.1175/2009JCLI3124.1.

Mayer, M., and L. Haimberger, 2012: Poleward atmospheric energy transports and their variability as evaluated from ECMWF reanalysis data. *J. Climate*, **25**, 734–752, doi:10.1175/JCLI-D-11-00202.1.

Monteith, J. L., 1965: Evaporation and environment. *Symp. Soc. Exp. Biol.*, **19**, 205–234.

Mueller, and Coauthors, 2011: Evaluation of global observations-based evapotranspiration datasets and IPCC AR4 simulations. *Geophys. Res. Lett.*, **38**, L06402, doi:10.1029/2010GL046230.

Nolin, A. W., R. Armstrong, and J. Maslanik, 1998: Near-Real-Time SSM/I-SSMIS EASE-Grid Daily Global Ice Concentration and Snow Extent, version 4. NASA National Snow and Ice Data Center Distributed Active Archive Center, doi:10.5067/VF7QO90IHZ99.

NSIT, 2007: A NASA Earth science implementation plan for energy and water cycle research: Predicting energy and water cycle consequences of Earth system variability and change. NEWS Science Integration Team Tech. Rep., 89 pp. [Available online at http://news.cisc.gmu.edu/doc/NEWS_implementation.pdf.]

Ohmura, A., and Coauthors, 1998: Baseline Surface Radiation Network (BSRN/WCRP): New precision radiometry for climate research. *Bull. Amer. Meteor. Soc.*, **79**, 2115–2136, doi:10.1175/1520-0477(1998)079<2115:BSRNBW>2.0.CO;2.

Onogi, K., and Coauthors, 2007: The JRA-25 Reanalysis. *J. Meteor. Soc. Japan*, **85**, 369–432, doi:10.2151/jmsj.85.369.

ORNL DAAC, 2013: Fluxnet web page. Accessed 1 July 2013. [Available online at http://fluxnet.ornl.gov.]

Peixoto, J. P., and A. H. Oort, 1992: *Physics of Climate*. American Institute of Physics, 520 pp.

Porter, D. F., J. J. Cassano, M. C. Serreze, and D. N. Kindig, 2010: New estimates of the large-scale Arctic atmospheric energy budget. *J. Geophys. Res.*, **115**, D08108, doi:10.1029/2009JD012653.

Reynolds, C. A., T. J. Jackson, and W. Rawls, 2000: Estimating soil water-holding capacities by linking the Food and Agriculture Organization soil map of the world with global pedon databases and continuous pedotransfer functions. *Water Resour. Res.*, **36**, 3653–3662, doi:10.1029/2000WR900130.

Rienecker, M. M., and Coauthors, 2008: The GEOS-5 Data Assimilation System—Documentation of versions 5.0.1 and 5.1.0, and 5.2.0. Tech. Rep. NASA/TM-2008-104606, 101 pp. [Available online at http://gmao.gsfc.nasa.gov/pubs/docs/Rienecker369.pdf.]

——, and Coauthors, 2011: MERRA: NASA's Modern-Era Retrospective Analysis for Research and Applications. *J. Climate*, **24**, 3624–3648, doi:10.1175/JCLI-D-11-00015.1.

Roads, J., M. Kanamitsu, and R. Stewart, 2002: CSE water and energy budgets in the NCEP–DOE Reanalysis II. *J. Hydrometeor.*, **3**, 227–248, doi:10.1175/1525-7541(2002)003<0227:CWAEBI>2.0.CO;2.

Roberts, J. B., C. A. Clayson, F. R. Robertson, and D. L. Jackson, 2010: Predicting near-surface characteristics from Special Sensor Microwave/Imager using neural networks with a first-guess approach. *J. Geophys. Res.*, **115**, D19113, doi:10.1029/2009JD013099.

Rodell, M., J. S. Famiglietti, J. Chen, S. Seneviratne, P. Viterbo, S. Holl, and C. R. Wilson, 2004a: Basin scale estimates of evapotranspiration using GRACE and other observations. *Geophys. Res. Lett.*, **31**, L20504, doi:10.1029/2004GL020873.

——, and Coauthors, 2004b: The Global Land Data Assimilation System. *Bull. Amer. Meteor. Soc.*, **85**, 381–394, doi:10.1175/BAMS-85-3-381.

——, and Coauthors, 2015: The observed state of the water cycle in the early 21st century. *J. Climate*, doi:10.1175/JCLI-D-14-00555.1, in press.

Rodgers, C. D., 2000: *Inverse Methods for Atmospheric Sounding*. World Scientific, 240 pp.

Rossow, W. B., and Y.-C. Zhang, 2010: Evaluation of a statistical model of cloud vertical structure using combined *CloudSat* and *CALIPSO* cloud layer profiles. *J. Climate*, **23**, 6641–6653, doi:10.1175/2010JCLI3734.1.

——, A. A. Lacis, and Y.-C. Zhang, 1995: Calculation of surface and top of the atmosphere radiative fluxes from physical quantities based on ISCCP data sets: 2. Validation and first results. *J. Geophys. Res.*, **100**, 1167–1197, doi:10.1029/94JD02746.

Schumacher, C., R. A. Houze Jr., and I. Kraucunas, 2004: The tropical dynamical response to latent heating estimates derived from the TRMM precipitation radar. *J. Atmos. Sci.*, **61**, 1341–1358, doi:10.1175/1520-0469(2004)061<1341:TTDRTL>2.0.CO;2.

Serreze, M. C., A. P. Barrett, A. G. Slater, M. Steele, J. Zhang, and K. E. Trenberth, 2007: The large-scale energy budget of the Arctic. *J. Geophys. Res.*, **112**, D11122, doi:10.1029/2006JD008230.

Shapiro, R., 1987: A simple model for the calculation of the flux of direct and diffuse solar radiation through the atmosphere. Tech. Rep. AFGL-TR-87-0200, 40 pp.

Slingo, A., and J. M. Slingo, 1988: The response of a general circulation model to cloud longwave radiative forcing. I: Introduction and initial experiments. *Quart. J. Roy. Meteor. Soc.*, **114**, 1027–1062, doi:10.1002/qj.49711448209.

Slingo, J. M., and A. Slingo, 1991: The response of a general circulation model to cloud longwave radiative forcing. II: Further studies. *Quart. J. Roy. Meteor. Soc.*, **117**, 333–364, doi:10.1002/qj.49711749805.

Stackhouse, P. W., Jr., S. J. Cox, S. Gupta, M. Chiacchio, and J. Mikovitz, 2001: The WCRP/GEWEX surface radiation budget project release 2: An assessment of surface fluxes at 1 degree resolution. *IRS 2000: Current Problems in Atmospheric Radiation*, W. Smith and Y. Timofeyev, Eds., A. Deepak Publishing, 24–29.

Stephens, G. L., and Coauthors, 2008: *CloudSat* mission: Performance and early science after the first year of operation. *J. Geophys. Res.*, **113**, D00A18, doi:10.1029/2008JD009982.

——, M. Wild, J. P. W. Stackhouse, T. L'Ecuyer, S. Kato, and D. S. Henderson, 2012a: The global character of the flux of downward longwave radiation. *J. Climate*, **25**, 2329–2340, doi:10.1175/JCLI-D-11-00262.1.

——, and Coauthors, 2012b: An update on the earth's energy balance in light of new surface energy flux estimates. *Nat. Geosci.*, **5**, 691–696, doi:10.1038/ngeo1580.

Su, H., and J. Jiang, 2013: Tropical clouds and circulation changes during the 2006/07 and 2009/10 El Niños. *J. Climate*, **26**, 399–413, doi:10.1175/JCLI-D-12-00152.1.

Susskind, J., J. M. Blaisdell, L. Iredell, and F. Keita, 2011: Improved temperature sounding and quality control methodology using AIRS/AMSU data: The AIRS science team version 5 retrieval algorithm. *IEEE Trans. Geosci. Remote Sens.*, **49**, 883–907, doi:10.1109/TGRS.2010.2070508.

Swenson, S., and J. Wahr, 2002: Methods for inferring regional surface-mass anomalies from Gravity Recovery and Climate Experiment (GRACE) measurements of time-variable gravity. *J. Geophys. Res.*, **107**, 2193, doi:10.1029/2001JB000576.

Tao, W.-K., S. Lang, J. Simpson, and R. Adler, 1993: Retrieval algorithms for estimating the vertical profiles of latent heat release: Their applications for TRMM. *J. Meteor. Soc. Japan*, **71**, 685–700.

Trenberth, K. E., 1983: What are the seasons? *Bull. Amer. Meteor. Soc.*, **64**, 1276–1282, doi:10.1175/1520-0477(1983)064<1276:WATS>2.0.CO;2.

——, 2009: An imperative for climate change planning: Tracking Earth's global energy. *Curr. Opin. Environ. Sustainability*, **1**, 19–27, doi:10.1016/j.cosust.2009.06.001.

——, and J. T. Fasullo, 2008: An observational estimate of inferred ocean energy divergence. *J. Phys. Oceanogr.*, **38**, 984–999, doi:10.1175/2007JPO3833.1.

——, and ——, 2013a: An apparent hiatus in global warming? *Earth's Future*, **1**, 19–32, doi:10.1002/2013EF000165.

——, and ——, 2013b: North American water and energy cycles. *Geophys. Res. Lett.*, **40**, 365–369, doi:10.1002/grl.50107.

——, and ——, 2013c: Regional energy and water cycles: Transports from ocean to land. *J. Climate*, **26**, 7837–7851, doi:10.1175/JCLI-D-13-00008.1.

——, J. M. Caron, and D. P. Stepaniak, 2001: The atmospheric energy budget and implications for surface fluxes and ocean heat transports. *Climate Dyn.*, **17**, 259–276, doi:10.1007/PL00007927.

——, J. T. Fasullo, and J. Kiehl, 2009: Earth's global energy budget. *Bull. Amer. Meteor. Soc.*, **90**, 311–323, doi:10.1175/2008BAMS2634.1.

——, ——, and J. Mackaro, 2011: Atmospheric moisture transports from ocean to land and global energy flows in reanalyses. *J. Climate*, **24**, 4907–4924, doi:10.1175/2011JCLI4171.1.

——, ——, and M. A. Balmaseda, 2014: Earth's energy imbalance. *J. Climate*, **27**, 3129–3144, doi:10.1175/JCLI-D-13-00294.1.

Vinukollu, R. K., E. F. Wood, C. R. Ferguson, and J. B. Fisher, 2011: Global estimates of evapotranspiration for climate studies using multi-sensor remote sensing data: Evaluation of three process-based approaches. *Remote Sens. Environ.*, **115**, 801–823, doi:10.1016/j.rse.2010.11.006.

Vonder Haar, T. H., and V. E. Suomi, 1969: Satellite observations of the earth's radiation budget. *Science*, **163**, 667–668, doi:10.1126/science.163.3868.667.

——, E. Raschke, M. Pasternak, and W. Bandeen, 1972: The radiation budget of the earth-atmosphere system as measured from the Nimbus 3 satellite. *Space Res.*, **12**, 491–498.

Wachtmann, R., 1975: Expansion of atmospheric temperature and moisture profiles in empirical orthogonal functions for remote sensing applications. Preprints, *Topical Meeting on Optical Remote Sensing of the Atmosphere*, Anaheim, CA, Optical Society of America.

Wang, K., and R. E. Dickinson, 2013: Global atmospheric downward longwave radiation at the surface from ground-based observations, satellite retrievals, and reanalyses. *Rev. Geophys.*, **51**, 150–185, doi:10.1002/rog.20009.

Wielicki, B. A., B. R. Barkstrom, E. F. Harrison, R. B. Lee III, G. L. Smith, and J. E. Cooper, 1996: Clouds and the Earth's Radiant Energy System (CERES): An Earth Observing System experiment. *Bull. Amer. Meteor. Soc.*, **77**, 853–868, doi:10.1175/1520-0477(1996)077<0853:CATERE>2.0.CO;2.

Wild, M., D. Folini, C. Schär, N. Loeb, E. G. Dutton, and G. König-Langlo, 2013: The global energy balance from a surface perspective. *Climate Dyn.*, **40**, 3107–3134, doi:10.1007/s00382-012-1569-8.

——, and Coauthors, 2015: The energy balance over land and oceans: An assessment based on direct observations and CMIP5 climate models. *Climate Dyn.*, **44**, doi:10.1007/s00382-014-2430-z.

Willis, J. K., J. M. Lyman, G. C. Johnson, and J. Gilson, 2009: In situ data biases and recent ocean heat content variability. *J. Atmos. Oceanic Technol.*, **26**, 846–852, doi:10.1175/2008JTECHO608.1.

Winker, D. M., and Coauthors, 2010: The *CALIPSO* mission: A global 3D view of aerosols and clouds. *Bull. Amer. Meteor. Soc.*, **91**, 1211–1229, doi:10.1175/2010BAMS3009.1.

Yu, J.-Y., and C. R. Mechoso, 1999: Links between annual variations of Peruvian stratocumulus clouds and of SST in the eastern equatorial Pacific. *J. Climate*, **12**, 3305–3318, doi:10.1175/1520-0442(1999)012<3305:LBAVOP>2.0.CO;2.

Zhang, Y.-C., W. B. Rossow, A. Lacis, V. Oinas, and M. Mishchenko, 2004: Calculation of radiative fluxes from the surface to top of atmosphere based on ISCCP and other global data sets: Refinements of the radiative transfer model and the input data. *J. Geophys. Res.*, **109**, D19105, doi:10.1029/2003JD004457.

——, ——, and P. W. Stackhouse, 2006: Comparison of different global information sources used in surface radiative flux calculation: Radiative properties of the near-surface atmosphere. *J. Geophys. Res.*, **111**, D13106, doi:10.1029/2005JD006873.

——, ——, and ——, 2007: Comparison of different global information sources used in surface radiative flux calculation: Radiative properties of the surface. *J. Geophys. Res.*, **112**, D01102, doi:10.1029/2005JD007008.

——, C. Long, W. Rossow, and E. Dutton, 2010: Exploiting diurnal variations to evaluate the ISCCP-FD flux calculations and radiative-flux-analysis-processed surface observations from BSRN, ARM, and SURFRAD. *J. Geophys. Res.*, **115**, D15105, doi:10.1029/2009JD012743.